Utrecht University
Department of Geosciences

MSc Thesis

Mineralogical changes with increased strain; insights from the shear zones in Cap de Creus, NE Spain

Author:
A.M. Rinia

Under supervision of
Prof. dr. Martyn Drury
Dr. Richard Wessels

September 2024

Abstract

Mineralogical changes with increased strain; insights from the shear zones in Cap de Creus, NE Spain

By A.M. Rinia

The Cap the Creus peninsula at the northeastern end of the Pyrenees consist of variscan LP-HT metasediments affected by a large network of greenschist shear zones. The age of these shear zones is still debated.
These shear zones provide excellent exposure for studying their petrology and structural characteristics. This research investigates the relation between petrology, geochemistry and strain in mylonites and adjacent country rock with samples from two localities at the Cap the Creus peninsula, named i) Cala Sardina, a larger-scale zone, and ii) Tudela, a smaller-scale zone. Samples were collected at varying distances from the shear zone to compare low- to high-strain mylonites. Optical microscopy, X-ray fluorescence, Scanning Electron Microscopy (SEM) and Energy Dispersive X-ray Spectroscopy (EDS) in combination with Automated Mineralogy (AM) software were used to determine mineral assemblages and bulk rock compositions (BRC). Proximal samples showed lower-grade, more hydrated mineral assemblages compared to distal ones, despite similar BRC. Through optical microscopy and SEM-phase mapping it is also observed that most of the retrograde overprinting of the mineral assemblage took place after shearing deformation. Thermodynamic modelling with Perple_X allowed for estimation of metamorphic conditions. Both localities showed higher grade metamorphic conditions overprinted by greenschist-facies conditions where the Tudela locality (at least partially) deformed under undersaturated conditions. Laser Ablation Inducted Coupled Plasma Mass Spectrometry (LA-ICP-MS) provided trace element data to study fluid interactions between shear zones and country rock. Mass transport values of -9.69% and +11.1% were observed over ~20 cm in Tudela samples, while Cala Sardina samples showed +8.14% mass transport over 100 cm.
It is concluded that water input through the shear zones appears essential for the retrograde overprinting of previous high-grade mineral assemblages, and that developed shear zones are likely good conduits of water to the surrounding country rock. This explains lower grade assemblages closer to the shear zone and the bulk of the retrograde overprinting happening after shearing deformation. Here the scale of the shear zone, rather than distance or strain, appears to influence the water throughput.
A final remark can be made about the age of the Cap de Creus shear zones; As retrograde overprinting appears to happen after the shearing deformation starts, the dating of retrograde white mica by Vissers et al. (2017) likely reflects a later stage of shearing or reactivation during this time, and not necessarily the initiation of these shear zones. This could indicate that the hypothesis of Druguet (2001) and Carreras (2001), which states that these shear zones originated during the later stages of the Variscan orogeny, is correct.

Acknowledgements

I would like to thank my supervisors, Richard Wessels and Martyn Drury, for the opportunity to work on this project and their support throughout the research and writing process. Special thanks to Richard for his guidance during meeting and assistance with the SEM and other analyses. I would also like to thank Richard, Martyn, Ernst Willingshofer and Hans van Melick for collecting the samples for this research in Cap de Creus during my absence. I would like to thank Hans in particular for helping with the automated mineralogy workflow and the Perple_X modelling.
Lastly, thanks to all the master students on the VMA 2nd-floor for the nice tea and walk-breaks, which provided the needed moment of relaxation during this project.

Table of Contents

1. Introduction

1.1 General introduction

The processes involved in localization of strain in the lithosphere are fundamental to our understanding of plate tectonics. Numerical modelling of mantle convection fails to produce plate like behavior unless a degree of strain localization is implemented (Platt and Behr, 2011). On outcrop scale strain localization is recognized in the form of shear zones, and studying these can give new insights into strain localizing mechanisms. Next to this the physical and chemical environments of rocks during metamorphism give insight into the geodynamic history of the earth's crust, thus also aiding in the better understanding of large-scale deformation.

Mineral assemblages and textures provide an indication of the conditions and strain a rock experienced. Methods to obtain these conditions from mineral assemblage rely on the principle that a mineral changes systematically with pressure and temperature. Thermodynamic databases and models provide the mathematical framework to constraining these pressure and temperatures based on observed mineral assemblages and bulk rock composition. Recent advances in the field of Scanning Electron Microscopy (SEM) in combination with software that determines the relative abundance of elements and classify these as different phases make it possible to create phase maps of rock-sample surfaces. After phases are classified and mapped the gathered chemical data can be used to calculate a composition of the mapped rock. This method thus allows for both structural (through the phase maps) and chemical analysis of rock-samples.

The Cap de Creus peninsula is part of the Variscan basement of the Pyrenees. It consists of LP-HT metasediments cut by (presumably) greenschist shear zones. Many papers are written about the geology of the Cap de Creus peninsula and the shear zones there in particular because of their exceptional outcrop quality and abundant structures. Papers of for example Fusseis et al. (2006), Carreras (2001), Druguet et al. (1997) and Piazolo (2002) give in detail descriptions of the geometry and mechanics of these shear zones. Some researchers have also investigated the metamorphic-history and conditions of the area, such as; Druguet (2001), van Melick (2021) and Kok (2022) but combining both geochemical and mineralogical with structural analysis has not yet been explored in these shear zones.

This study aims to provide insight into the relation between petrology, geochemistry, and strain in mylonites and adjacent country rock. This will be done by structural, chemical and mineralogical analysis of multiple samples taken from lithological layers at various differences from, and thus deformed by, shear zones using optical microscopy, Scanning Electron Microscopy, thermodynamic modelling and trace element analysis.

1.2 Geological setting

The Pyrenees are an intracontinental mountain belt formed by the partial subduction of the Iberian plate underneath the European continent from the Early Eocene until the late Oligocene. The mountain belt consists of the North Pyrenean thrust system, the Axial zone and the South Pyrenean thrust system (fig. 1.1). These zones are separated by large scale faults formed during Alpine movements; the North Pyrenean Fault between the North Pyrenean thrust system and the axial zone, and the Nogueras zone between the axial zone and the South Pyrenean thrust system (fig. 1.1) (Vergés et al., 2002; Choukroune, 1992).
The basement of the Pyrenees, the axial zone, consists of rocks from the Cambro-Ordovician to Carboniferous that are deformed and metamorphosed by the Variscan orogeny during the Carboniferous (Zwart, 1979). The basement is surrounded by the Northern and Southern Pyrenean thrust systems which deformed Mesozoic rocks during the Alpine orogeny (Choukroune, 1992).

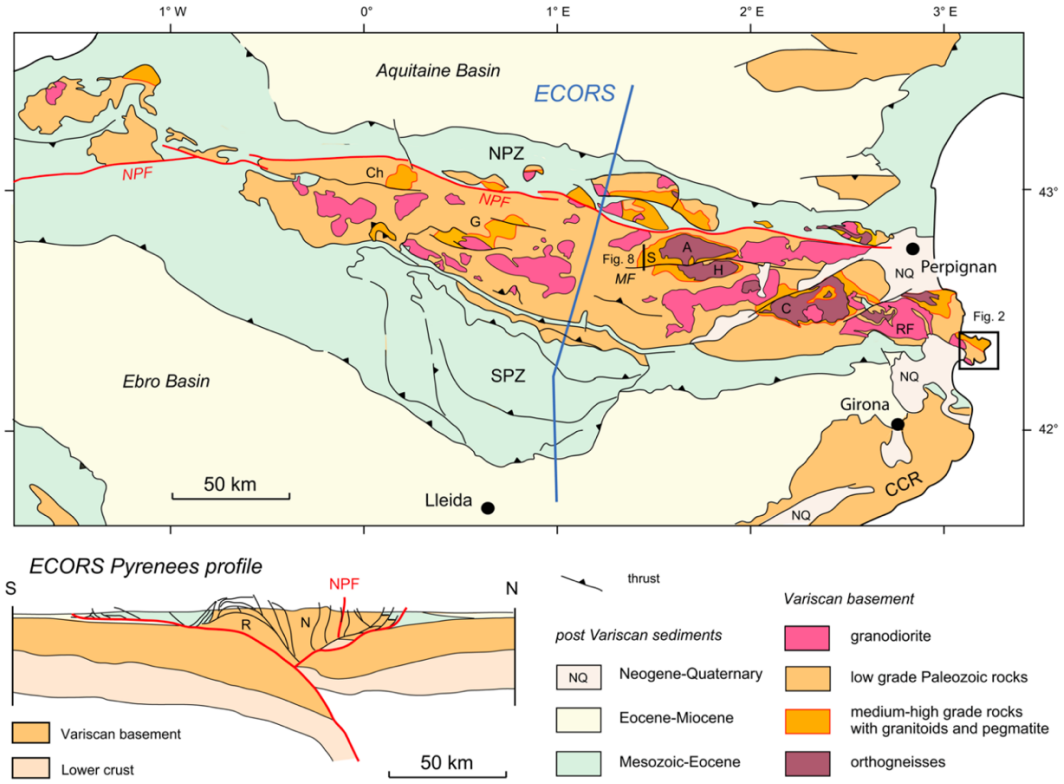

Fig. 1.1 Geological map of the Pyrenees taken from (Vissers et al., 2017). NPZ= North Pyrenean thrust system, NPF= North Pyrenean Fault, SPZ= South Pyrenean thrust system. The Cap de Creus area is located in the square denoted with Fig.2.

The axial zone is made up of folded and metamorphosed sediments and various granitoid bodies. In these metamorphosed sediments there is a distinction between i) a low-grade domain, which is dominated by steep folds in slates and phyllites, and ii) a medium- to high-grade domain dominated by mica schists, migmatites and gneisses in recumbent folds and flat lying foliation. Most of the axial zone underwent lower greenschist or sub-greenschist facies metamorphism, while the local high-grade domains are metamorphosed up to amphibolite facies (Zwart, 1986; Carreras and Capella, 1994). Steep dipping thrusts and strike-slip faults, both with large vertical components, cut the axial zone. These faults have both Variscan and Alpine ages (Mezger et al., 2012).
Various sized bodies of intrusive granodiorite are present in the axial zone, usually in contact with lower grade sediments characterized by large contact-metamorphic aureoles. These bodies are related to the Variscan orogeny (Zwart, 1986; Filleaudeau et al., 2012).

1.2.1 Cap de Creus metamorphism and magmatism

The Cap de Creus peninsula (Fig. 1.2) is the easternmost part of the Pyrenean mountain belt and is a part of the axial zone. The geology of this area consists of greenschist to amphibolite-facies metasediments and granitoid bodies (Zwart, 1979; Carreras, 2001).

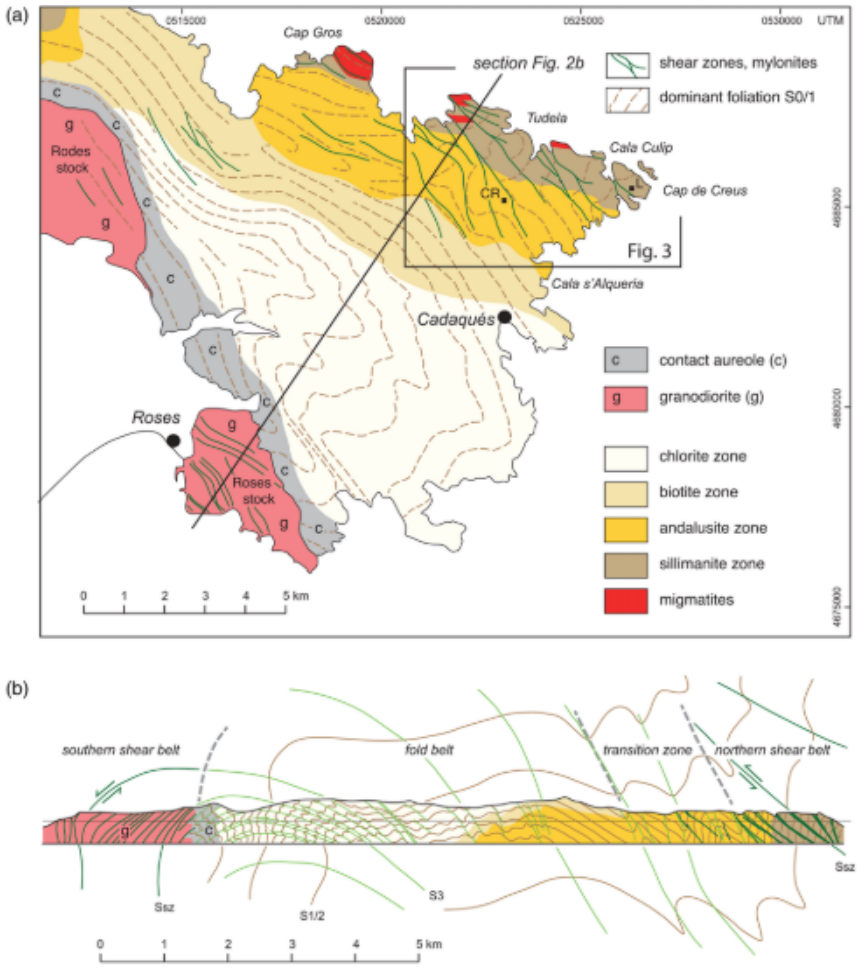

Fig. 1.2: Structural sketch of the Cap de Creus area taken from Vissers et al. (2017). (a) shows a map in which metamorphic zones are sketched, (b) shows a structural cross section of the peninsula in which large scale deformation and direction is sketched .

The metasediments in this area are dominantly psammitic and pelitic rocks, occasionally enclosing layers of quartzite. The suggested age of these metasediments is Late Proterozoic to Cambrian (Castiñeiras et al., 2008). The metasediments show a LP-HT field gradient over a distance of 2-3km, ranging from a chlorite-muscovite zone in the southwest to a sillimanite-K-feldspar zone with local migmatites in the northeast (fig. 1.2a) (Druguet et al., 2001). The area has a, still debated, metamorphic field gradient of around ~80°C/km (Druguet, 2001).

All the metamorphic zones present in the area from SW to NE, after (Druguet, 2001), are:

- **Chlorite-muscovite zone**: very low to low metamorphic grade, phyllites and meta-grey wackes.
- **Biotite zone:** Phyllites to mica-schist with macroscopic biotite assemblages.
- **Andalusite-cordierite zone**: Larger-grained mica-schist with cordierite + andalusite porphyroblasts.
- **Sillimanite-k-feldspar zone**: Further increase in grainsize, sillimanite mainly growing as fibrolite associated with quartz nodules.
- **Migmatites**: (partially) migmatised sillimanite-schist.

The focus of this research is on the high-grade sillimanite-muscovite and the migmatite zones. The sillimanite zone has a mineral assemblage of quartz, biotite, plagioclase, muscovite, sillimanite, cordierite and/or k-feldspar. Thermobaric calculations estimate P-T conditions for this zone at 2.4-4.7 kbar and 560-670 °C (Druguet, 2001). Not many PT-estimates have been made for the rocks in the migmatite complex. Druguet (1997) suggests temperatures above 700 °C and pressures up to 7.4 kbar, which represents a very large pressure step compared to the adjacent sillimanite zone. Research done by Kok (2022) suggests conditions of ~700 °C and 4.5-5.0 kbar, where further research to more precisely estimate the PT conditions is suggested.

There are two groups of intrusive rocks in the Cap de Creus area:
i) the larger Roses and Rodes intrusions. These intrusions have a homogeneous composition, varying between granodiorite and tonalite. They are sheet-shaped and emplaced in the lower grade metasediments, producing an aureole of contact metamorphism (Druguet, 2001). These features have been interpreted to indicate shallow depths of intrusion (Carreras and Losantos, 1982). U/Pb zircon-dating has yielded 299-291 Ma (Variscan) age for these granodiorite intrusions (Druguet et al., 2014).
ii) The second and smaller group of intrusions are located in the northern sillimanite-muscovite and sillimanite-k-feldspar zones. They consist of small intrusions of hornblende quartz-gabbro, quartz-diorite, tonalite, granodiorite, granite and dykes of leucogranite and pegmatite. The pegmatites are the youngest intrusions and form a 2.4 km wide irregular dyke swarm from the cordierite-andalusite to the sillimanite zone (Druguet, 2001).

1.2.2 Cap de Creus deformation

The Cap de Creus area has a polyphase deformation history with three main deformation episodes:

D1) This oldest deformation phase resulted in widespread schistosity (S1, fig. 1.2b), which is well defined in the metasedimentary rocks by alignment of phyllosilicates. This event resulted in recumbent folds and thrusts with gently dipping foliation, interpreted to result due to crustal thickening and associated metamorphism (Druguet 2001).

D2) The D2 event is characterized by the folding of bedding and the S1 schistosity under prograde metamorphic conditions (up to peak metamorphism). The D2 structures evolved to folds and crenulation cleavages with a now E-W trend (S2, fig. 1.2b). F2 folds are characterized by vertical or steeply inclined axial surfaces and associated crenulation cleavage (Druguet, 2001). Previous works of Druguet (1997) and Carreras and Druguet (1994) suggest this event resulted in a complex transpressive shear zone involving vertical extensions.

D3) The third deformation event occurred under retrograde greenschist metamorphic conditions. This event overprints the D1 and D2 structures by shearing and folding them. Orientation of the D3 folds and shear zones is roughly NW-SE, rotating more towards NNW-SSE with increasing strain (S3, fig. 1.2b) (Druguet, 2001; Carreras, 2001).

1.2.3 Cap de Creus Northern Shear belt

In higher metamorphic grade domains the D3 late folds (mentioned in 1.2.2) disappear and shear zones become more prominent and form anastomosing networks (fig. 1.3) (Druguet, 2001). These networks are separated into two major belts by Carreras (2001); the northern and southern shear belts. These are WNW-ESE trending shear belts and are part of the mylonite belts in the Axial zone. The focus of this research is on the northern Cap de Creus shear belt.

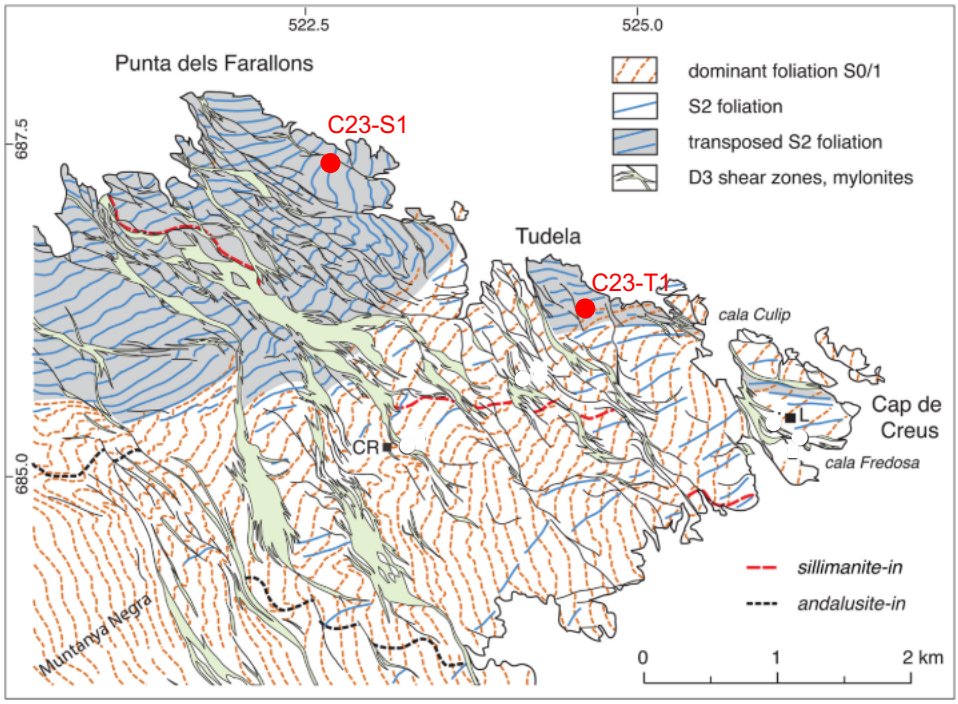

Fig. 1.3: Structural map of the northeastern part of the Cap de Creus peninsula and the Northern shear belt, taken and adjusted from Vissers et al. (2017). Sampling localities from this research noted in red dots; C23-S1 locality called "Cala Sardina" and C23-T1 locality called "Tudela".

The northern shear belt is made up of multi-scale anastomosing shear zones (cm to meter scale) characterized by dextral shear along NE-plunging stretching lineations. This belt obliquely cuts the medium to high-grade foliated schists (S1 and S2) (fig. 1.3) (Carreras, 2001; Vissers et al., 2017). Shear zone formation occurred at lower greenschist facies metamorphic conditions, at the brittle to viscous transition zone in the crust (Carreras. 2001; Fusseis et al., 2006). Re-equilibration of minerals is commonly observed in mylonites, with new growth of muscovite, albite, epidote, chlorite and recrystallization of quartz (Carreras, 2001).

As a results of the lithological heterogeneity in the area, two types of mylonite occur in the shear belt. These are (Carreras, 2001);
i) Mainly quartz-feldspathic and mica-rich mylonites, derived from metagreywacke and metapelitic protoliths. Thin quartz band are commonly observed in these mylonites and result from the presence of quartz segregation veins and nodules in the schist protolith. These quartz-mylonites exhibit well-marked stretching lineations defined by the alignment of elongated mineral crystals and intersection lineation.
ii) A leucocratic quartz-feldspatic mylonite derived from the pegmatites and leucogranites found in the area.

Geological age of these shear belts was previously assumed as late-stage Variscan, based on structural data from the area (Carreras, 2001; Druguet, 2001; Druguet et al., 2014). But this age has been questioned by Vissers et al. (2017) who suggest an Alpine age based on Ar/Ar dating of muscovite grains in the shear zones. This has sparked a debate between researchers (Druguet et al., 2018; Vissers et al., 2018), in which no consensus has yet been reached.

1.3 Shear zone mechanics

A shear zone, as defined by White et al. (1980), is "a planar zone of concentrated, dominantly simple shear deformation which helps to accommodate or wholly accommodates an imposed regional or local strain rate which the country rock cannot accommodate by bulk deformation". Shear zones are thought to initiate at microscale flaws or from larger scale structures such as fractures or dykes, from which they form displacement profiles similar to faults (Pennacchioni and Mancktelow, 2007). Like faults, they are zones of strain localization, but they differ from brittle faults in their continuous displacement and/or ductile behavior. They grow in width and length by segment linkage as strain and displacement accumulate (Pennacchioni, 2005). Thus, they range from the scale of a small outcrop to km-scale anastomosing networks.
Ductile shear zones are likely formed at the brittle-to-viscous transition in the earth's crust (Fusseis et al., 2006; Carreras et al., 2010). The dominant deformation mechanisms in these shear zones are crystal-plastic mechanisms (dislocation creep and twinning) and diffusion. Crystal plasticity is controlled by mineralogy, temperature and pressure, presence of fluids, strain rate and grain size (Fossen and Cavalcante, 2017)

Processes that are involved in strain localization in shear zones are dissipative heating, development of lattice preferred orientation (LPO) and grainsize reduction by cataclasis or dynamic recrystallization (Platt and Behr, 2011; Watts and Williams, 1983; White, 1979). Dynamic recrystallization, i.e. recrystallization during shearing, usually softens the rheological properties of the rock (Fossen and Cavalcante, 2017). Recrystallization typically leads to the development of a LPO, which puts mineral grains in orientations of easy slip and thus weakens the rock, which is known as geometric softening (Passchier and Trouw, 2005).

Metamorphic growth of weak mineral phases during shearing, such as mica growth on behalf of feldspar, is another weakening factor known as reaction softening (Passchier and Trouw, 2005). Hydrolytic weakening is caused by the introduction of water into the crystal lattice. It reduces the intracrystalline rock strength, facilitates dissolution precipitation and accelerates grain boundary migration and grain boundary sliding (wet quartz has lower differential stress that dry quartz). Shear heating increases the temperature enough to weaken the internal part of the shear zone, where additional partial melting in migmatitic areas can create melt that has a lubricating effect as well (Gibson, 1990).

1.4 Aims and Scope

The shear zones at Cap de Creus allow for insights into the evolution of a crustal-scale shear zone network, formed in foliated metasedimentary rocks under greenschist-faces conditions. They also offer a unique opportunity to study the progressive development of fabrics with increasing strain.
This study aims to show insight into the relation between petrology, geochemistry, and strain in mylonites and adjacent country rock. We will compare samples from metasedimentary layers that have been exposed to different amounts of strain (the same lithological layer closer and further away from the shear zone). These samples will be studied on structures and composition using microscopy, Scanning Electron Microscope (SEM) Energy Dispersive X-ray Spectroscopy (EDS) automated mineralogy analysis, X-ray Fluorescence Spectroscopy (XRF), and Laser Ablation (LA) Inductively Coupled Plasma Mass Spectrometry (ICP-MS).

2. Approach and Methodology

2.1 Fieldwork

Fieldwork was conducted to acquire the samples needed for this research. Sampling took place in the north-western Cap de Creus area where two different parts of the northern shear zone were sampled for further analysis at Utrecht University.

Each sampling consisted of the following steps: i) overview photo's before and after sampling, ii) detailed systematic set of photo's covering the sampling area, iii) marking the orientation of the sample, the foliation, lineation, and highest corner (following Tikoff et al., 2019) measurements of the foliation and lineation, v) measurements of the shear zone orientation, width, and (apparent) offset.

The first sampling location is part of a migmatite-zone in the north-western part of the Cap de Creus peninsula called Cala Sardina (see map fig. 1.3). Samples were taken from one mylonitic layer affected by a meter-scale shear zone (fig. 3.1). Four different hand-samples were taken, at different distances from the shear zone (fig. 3.1 and 3.3), named C23-S1-A to C23-S1-D. From these hand-samples thin sections were cut in a horizontal XZ plane perpendicular to the foliation, following the method by Tikoff et al. (2019). All thin sections are downward facing, i.e. looking down into the outcrop.

The second sampling region is located in the Tudela area, which is part of the sillimanite zone. The mylonitic layers in this area were affected by a smaller cm-scale shear zone (see fig 3.2). A part of the shear zone was photographed and taken for sampling as a whole, allowing for reconstruction of the outcrop in the lab (fig. 3.2 right). Two of the affected metasedimentary layers were selected for further inspection and cut into thin sections. Samples from these two layers are named C23-T1-A to C23-T1-I. Thin sections were cut perpendicular to foliation and parallel to the horizontal, which is almost parallel to the shear zone lineation in this locality. All thin sections are downward facing, i.e. looking down into the outcrop, except for thin section C23-T1-E, which is upward facing. Locations of thin sections are denoted in figure 3.2 right.

For each sampled section a value of applied shear strain was calculated. This was done using the angle between the undeflected and deflected foliation and the shear plane by applying the formula:

$$\gamma = \cot \alpha' - \cot \alpha$$

Where the angle between the undeflected foliation and the shear plane is α, the angle between the deflected foliation and shear plan is α' and the calculated applied shear strain is γ (Fossen and Cavalcante, 2017).

2.2 Digitizing thin sections and Optical microscopy

The thin section from both shear zones were scanned and digitized using a Zeiss Axio Scan.Z1 thin section scanner. High-resolution scans of 0.44 μm/pixel were made using a 10x magnification and brightfield transmitted light. Each thin section scan contains one image of plane polarized light, and six images of cross polarized light each rotated 15° from the last. Interpretation and annotation of scans was done using ZEN 3.2 virtual microscopy software. Additional optical microscopy with a traditional petrological microscope of the thin sections allowed for the study of relief and pleochroism, aiding in the identification of minerals in the samples.

2.3 Scanning Electron Microscopy and Automated Mineralogy

A Scanning Electron Microscope (SEM) in combination with an Automated Mineralogy program (AM) will be used to obtain the rock chemistry for several samples of different strain-levels.
The SEM-images were made using a Zeiss EVO-15 electron microscope with two Bruker XFlash 6|60 detectors and one backscattered electron (BSE) detector. The accelerating voltage was set to 15 KV and the probe current was set on 1 nA for all samples, this allowed for identification of all necessary elements in the samples.
The Bruker Esprit v2.1 software was used for energy dispersive X-ray spectroscopy spot measurements on all the different mineral phases in the sample. The spot measurements provide the chemical composition of the phases and allowed for the identification of their mineralogy, which was used as input for the automated mineralogy workflow.
Using the Zeiss Mineralogic v1.08 software a region of interest was selected on each sample. Each pixel in the region of interest was scanned for chemical composition and converted to a phase, resulting in a phase map. The Zeiss Mineralogic software also provides the area percentage, weight percentage, and average chemical composition in normalized atomic mass for each phase.
A python script written by van Melick, 2021 that uses mineral compositions to calculate bulk rock composition was then used to compare the bulk rock compositions resulting from the automated mineralogy against the compositions determined using the spot measurements, as a means of quality control.

2.4 XRF

X-ray Fluorescence (XRF) analysis was performed on all samples in order to obtain a bulk rock composition. For the samples also analyzed using the SEM-AM workflow this measurement was used as a second independent check.
The analyzed material used is cut from the same plane from which the corresponding thin section was cut, allowing a direct comparison of the results. This material is grinded to powder and dissolved in a heated borate flux, before being cooled into glass beads, to achieve homogeneity. The analysis of these samples was conducted on a Thermo Scientific ARL Perform 'X 4200W WDXRF analyzer.

2.5 LA-ICPMS

Next to the BRC-analysis a trace element analysis was performed on all samples. Trace element concentrations provide insight into the amount of alteration that a rock has undergone due to fluid mass transfer.
In order to obtain reliable data on the elemental concentrations (down to ppm) the samples were analyzed using LA-ICP-MS, laser ablation inductively coupled plasma mass spectrometry. All samples were analyzed three times with the same configurations. The mean values of these three measurements were used to calculate concentration ratios. The data has been calibrated using the BCR-2G standard and processed using the GLITTER software (Griffin et al., 2008).

The method used for the further analysis of this data gives an insight into the overall change in rock mass when comparing the distal and proximal samples in this study. The method is described in Philpotts and Ague (2009) and Ague (2003) and relies on the assumption that immobile elements are unaffected by fluid transport. Immobile elements include high field strength elements (Hf, Zr, Ti, Nb, Ta and Th) and rare earth elements (Philpotts and Ague, 2009). Immobile elements are used to calculate an average immobile concentration ratio C/Ci (concentration of an element in an altered rock compared to concentration of that same element in an unaltered rock), which indicates the degree to which mobile elements have been

transported. Here the “altered rock” is the sample locality closest to the shear zone and the “unaltered rock” is the sample locality furthest from the shear zone.
For all mobile elements a C/Ci-ratio is calculated as well to obtain information on the element having been added or removed from the rock all these values and the average immobile C/Ci ratio are plotted in a graph. Lastly the total transported mass (so all mass that was lost and added together) is calculated using the formula:

$$T_{mass,i} = \frac{c_i^0}{c_i'} - 1$$

Where $T_{mass,i}$ is the total transported mass of a reference immobile element i, c_i^0 is the concentration of that element i in the unaltered rock and c_i' is the concentration of i in the altered rock (Philpotts and Ague, 2009). Here T<0 of the rock has lost mass and T>0 if mass was gained. All total mass transports of all immobile elements are then used to calculate a total mass gain or loss for each sampled layer.

2.6 Thermodynamic modelling

The Perple_X software package (Connolly and Petrini, 2002; Connolly, 2005; Connolly and Galvez, 2018) version 6.9.0 (https://www.perplex.ethz.ch) with the dataset hp62ver.dat of Holland and Powell (2011) was used to calculate equilibrium mineral assemblages for a selection of the samples. Solution models for biotite, chlorite, chloritoid, cordierite garnet, staurolite and white mica from White et al., (2014) and feldspar form Holland and Powell (2011) (all calibrated with the used thermodynamic dataset) were used. The chemical system that was considered included: MnO, Na2O, CaO, K2O, Fe2O3, MgO, Al2O3, SiO2, TiO2, and assuming the fluid phase to be pure H2O. P-T psuedosections were redrawn and annotated using Adobe Illustrator.

3. Results

Sample location	Sample name	TS	OM	SEM-AM	XRF	LA-ICP-MS	Perple_X
Cala Sardina	C23-S1-	A	X	X	X	X	X
		B	X		X	X	
		C	X		X	X	
		D	X	X	X	X	X
Tudela	C23-T1-(red layer)	A	X	X	X	X	X
		B	X		X	X	
		C	X		X	X	
		D	X		X	X	
		E	X	X	X	X	X
	C23-T1-(green layer)	F	X		X	X	
		G	X		X	X	
		H	X		X	X	
		I	X	X	X	X	X

Table 3.1: Overview of samples and analyses performed. OM=Optical Microscopy, SEM-AM=Scanning Electron Microscope and Automated Mineralogy, XRF= X-ray Fluorescence, LA-ICP-MS=Laser Ablation.

For this research a total of 13 thin sections from 3 distinct lithological layers have been studied. Table 3.1 shows an overview of the thin sections/samples and the applied analytical and numerical methods.

3.0 Description of field relations

The results section 3.0 contains a description of the field relations and the calculated shear strain for the selected Cala Sardina and Tudela shear zone sample localities.

3.0.1 Cala Sardina

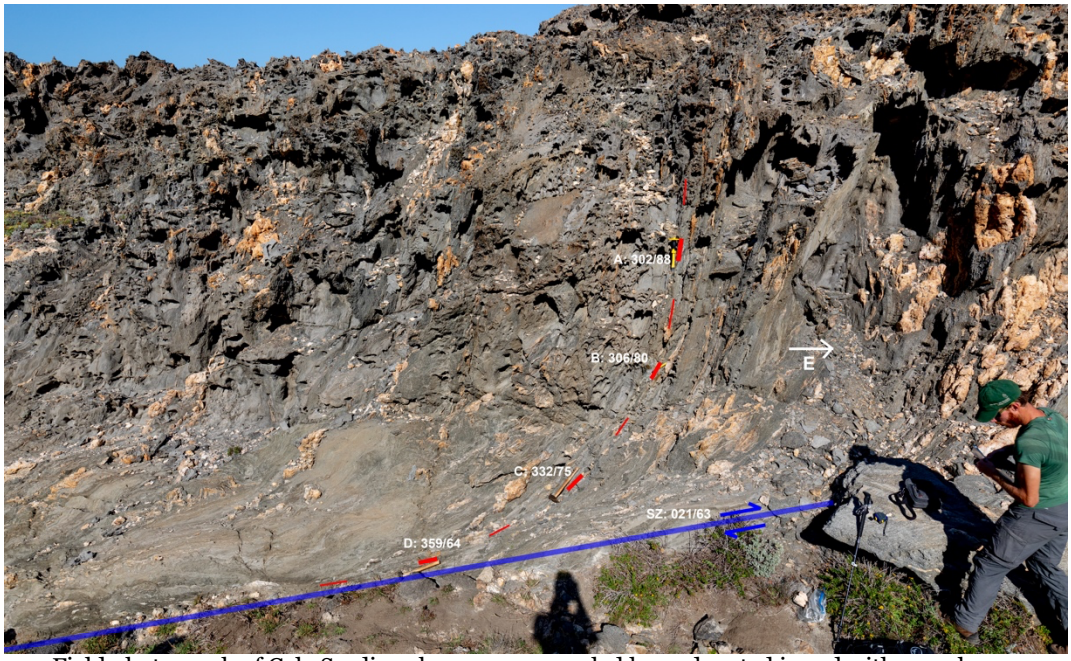

Figure 3.1: Field photograph of Cala Sardina shear zone, sampled layer denoted in red with sample names and dip direction/dip measurements, shear zone annotated in blue, thesis supervisor for scale. Shear sense is dextral.

Measurement	Distance to shear zone	Dominant foliation	Shear strain (calculated)	Associated thin section
Fol. undisturbed		308/88	0.0	
CS-A	100 cm	302/88	0.0	C23-S1-A
CS-B	70 cm	306/80	0.1	C23-S1-B
CS-C	45 cm	332/75	1.1	C23-S1-C
CS-D	12 cm	359/64	3.2	C23-S1-D
Shear zone fol.		021/63		
Shear zone lin.		085-41		

Table 3.2: Measured foliation/lineation and calculated shear strain values for the Cala Sardina samples.

To calculate the strain imposed on each studied sample, orientation of the dominant foliation at sampled locations and measurements of the shear zone foliation and lineation were taken (figure 3.1). Shear strain was calculated, as shown in the method section, using the angle between the undeflected and deflected foliation and the shear zone. Calculated shear strain values are noted in table 3.2. Shear strain increases from zero for location C23-S1-A at one meter from the shear zone boundary towards a value of 3.2 for location C23-S1-D at 12cm from the shear zone boundary.

3.0.2 Tudela

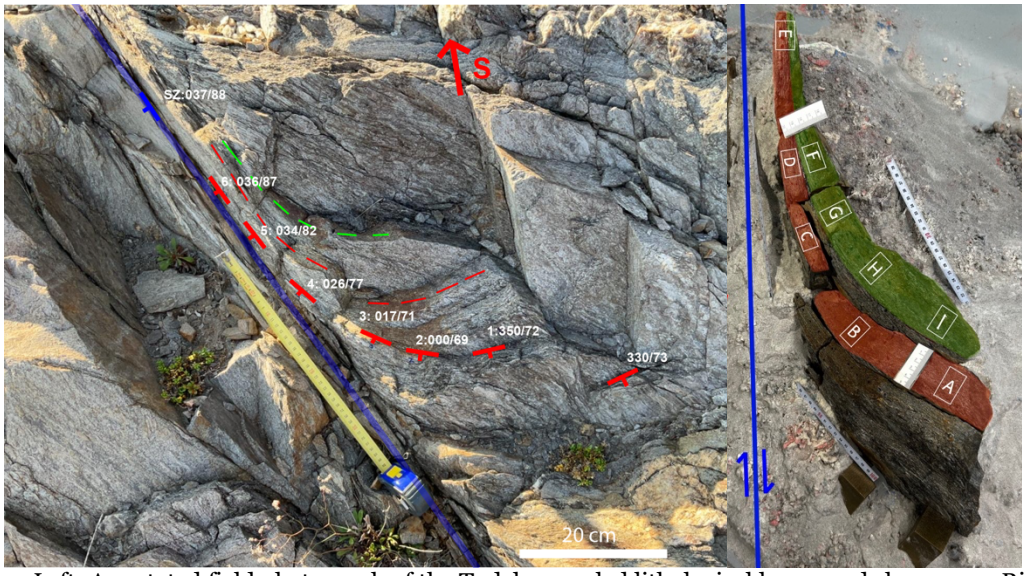

Figure 3.2: Left: Annotated field photograph of the Tudela sampled lithological layers and shear zone. Right: Top view of sampled layers from the Tudela locality rebuilt in Utrecht Earth Simulation Laboratory, thin section locations annotated. Shear sense is dextral.

Measurement	Distance to shear zone	Dominant foliation	Shear strain (calculated)	Associated thin section(s)
Fol. undisturbed		330/73	0.0	
T-1	20 cm	350/72	0.7	
T-2	13 cm	000/69	1.3	C23-S1-I and C23-S1-A
T-3	9 cm	017/71	3.8	C23-S1-H and C23-S1-B
T-4	3 cm	026/77	9.0	C23-S1-G and C23-S1-C
T-5	1 cm	034/82	56.8	C23-S1-F and C23-S1-D
T-6	<1 cm	036/87	114.1	C23-S1-E
Shear zone fol.		037/88		
Shear zone lin.		308-20		

Table 3.3: Measured foliation/lineation and calculated shear strain values for the Tudela area.

The same method for calculating shear strain was applied to the Tudela shear zone. As the samples were taken from the extracted block in the laboratory at Utrecht University, there is only an approximate match between measured dominant foliation in the field and the location of the samples (figure 3.2 and 3.3). Table 3.3 shows the measured foliation and associated imposed shear strain. Shear strain increases from a value of zero at 20cm distance from the shear zone boundary, through 1.3 (C23-S1-I and C23-S1-A) at 13cm, up to 114.1 (C23-S1-E) at a distance of <1cm from the shear zone boundary.

The following result section (3.1) contains a description of the samples taken at the Cala Sardina and Tudela localities, including petrology based on optical microscopy.

3.1 Sample description

3.1.1 Cala Sardina

Four samples were taken from the Cala Sardina shear zone (see fig. 3.1 and fig. 3.3).
The bulk of the mineral assemblage observed using optical microscopy in all thin sections is quartz, biotite, muscovite, chlorite, sillimanite and plagioclase.
Three main features are visible in these thin sections (fig. 3.3 and 3.4):

- Folded quartz veins of up to 1mm thickness
- Matrix of quartz, plagioclase, biotite, sillimanite, muscovite and chlorite. The phyllosilicates are often banded together. Sillimanite is found in patches of fibrolite, usually growing over quartz (figure 3.7).
- Nodules of muscovite up to mm size.

In the samples furthest from the shear zone (C23-S1-A fig 3.3, and C23-S1-B) quartz veins and phyllosilicate bands are clearly visible, defining a dominant foliation and a crenulation foliation, these two foliations have an angle of around 120° (fig. 3.3). The core of the muscovite nodules consists of epidote. All banded muscovite in the matrix shows the same CPO which differs from the CPO of the muscovite nodules.
Moving closer to the shear zone (C23-S1-C and C23-S1-D fig 3.3) the quartz veins become smaller and eventually are completely broken up into grains, average quartz grain size decreases, from ~0.5 mm in section C23-S1-A to ~0.1 mm in C23-S1-D. The muscovite nodules remain intact with a relatively constant size (~ 1mm). Phyllosilicates also remain around the same size from C23-S1-A to C23-S1-D, while the density of phyllosilicate bands increases. Towards the shear zone the dominant foliation becomes overprinted by the crenulation foliation, with parallelism between both foliations increasing with proximity towards the shear zone (fig. 3.3).

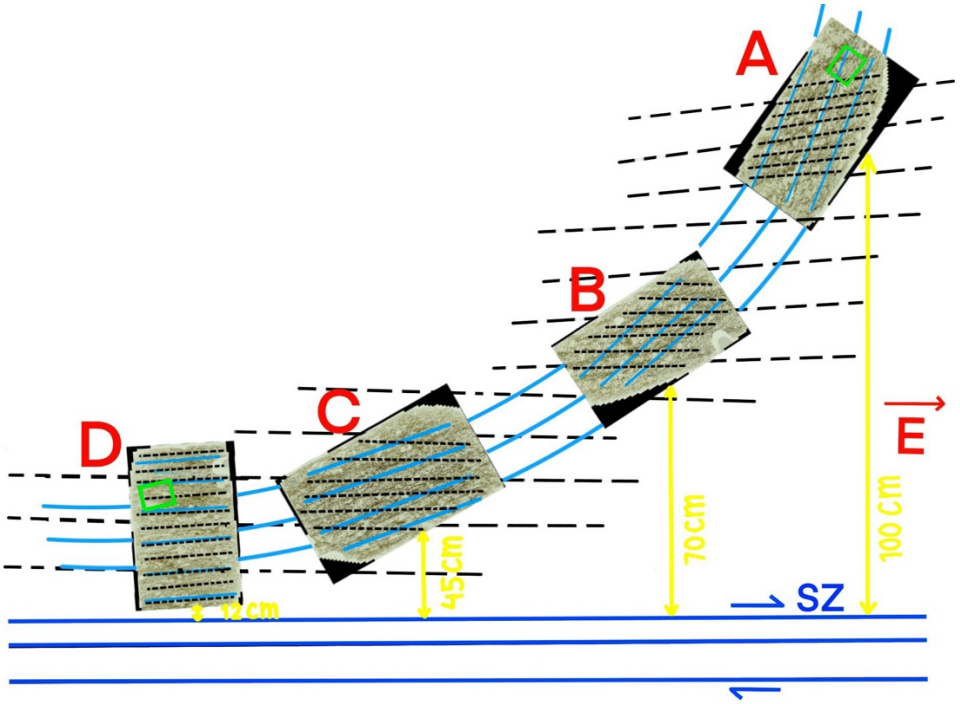

Figure 3.3: Situation sketch of the Cala Sardina locality and the thin section made from the sample points. For real scale view figure 3.1. First dominant foliation annotated in blue, crenulation foliation in black dotted lines. Green boxes show locations of close ups in figure 3.4 and 3.6.

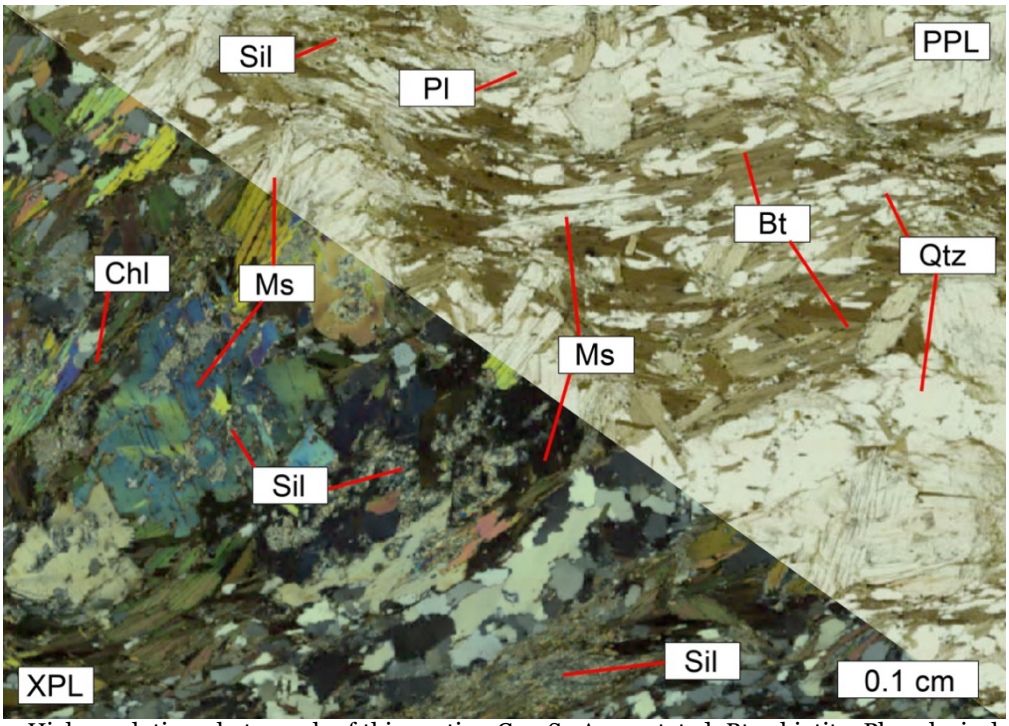

Figure 3.4: High resolution photograph of thin section C23-S1-A annotated. Bt = biotite, Pl = plagioclase, Qtz = quartz, Sill = sillimanite, Ms = muscovite, Chl = chlorite. Quartz veins and banded phyllosilicates define dominant and crenulation foliations.

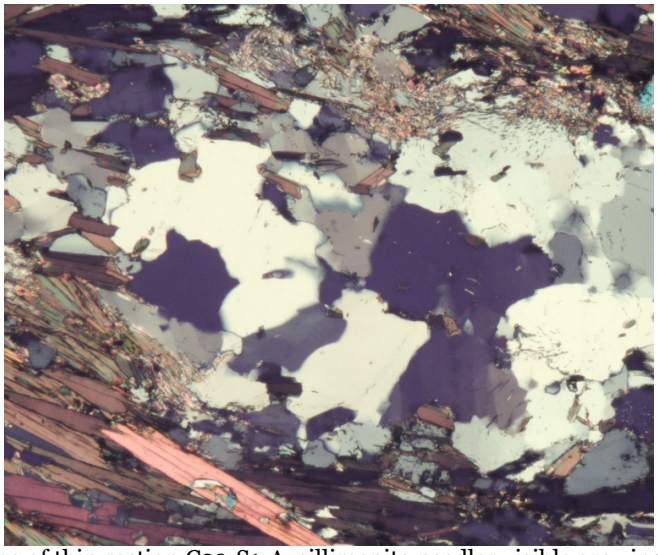

Figure 3.5: Close up picture of thin section C23-S1-A, sillimanite needles visible growing over quartz grains in top right corner.

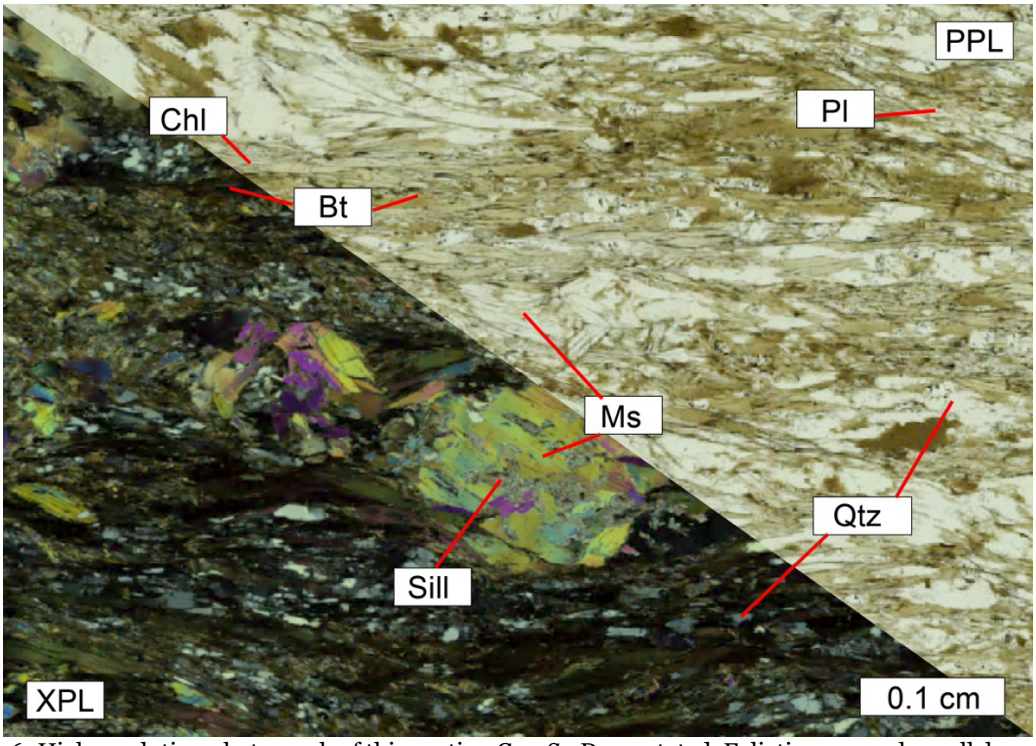

Figure 3.6: High resolution photograph of thin section C23-S1-D annotated. Foliations are subparallel.

3.1.2. Tudela

Nine samples were taken from two adjacent lithological layers in the Tudela shear zone. These two layers have a very similar mineral content and structure and thus both are described in this section.

The majority of the samples is made up of; quartz, plagioclase, biotite, orthoclase, sillimanite and muscovite. Secondary minerals include apatite, tourmaline and albite.

The main features in the Tudela samples are:

- Matrix of plagioclase, quartz grains and banded biotite, with some areas also containing sillimanite.
- Bands of biotite and plagioclase, with almost no quartz
- Clusters of orthoclase, sometimes combined with muscovite and sillimanite

In the samples furthest from the shear zone, samples T1-A and T1-I (fig. 3.5), the dominant spaced foliation (figure 3.7) is mostly defined by the aligning of biotite grains. These biotite bands are poorly connected and often wrap around clusters of plagioclase and quartz minerals, with locally muscovite and sillimanite.
Closer to the shear zone the quartz and phyllosilicate grains are deformed and their grain size decreases, quartz grains decreasing from ~0.2 mm in section C23-T1-A to ~0.01mm in C23-T1-E. The bands of sillimanite disappear with only sparse small clusters remaining. Clusters of orthoclase start to break up and closest to the shear zone disappear completely.
In the thin section taken closest to the shear zone (T1-E fig 3.6) the dominant foliation is a crenulation foliation (figure 3.7) and is defined by biotite, muscovite and quartz grains in undulating shear bands. Plagioclase grains remain more intact compared to the other minerals, which wrap around them. Orthoclase has almost entirely disappeared in this thin section and only a few clusters of sillimanite and muscovite can be observed.

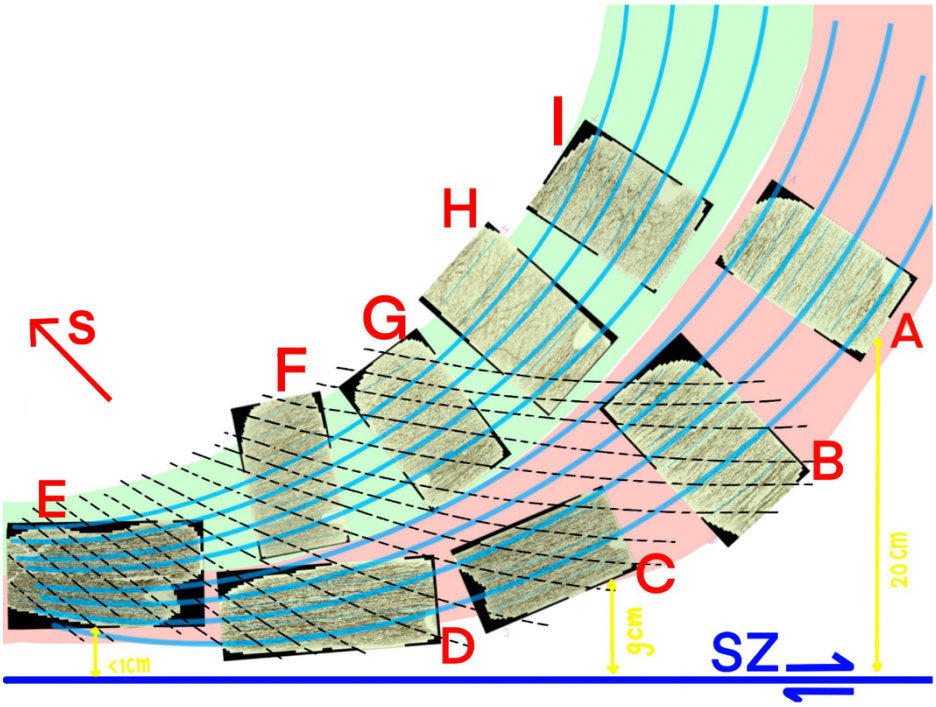

Figure 3.7: Situation sketch of the Tudela shear zone and sampled layer and thin sections, for real scale and more accurate distance between thin sections view figure 3.2. Dominant foliation sketched in blue and crenulation cleavage in dashed black line. Thin section C23-T1-H, C23-T1-I and C23-T1-A do not clearly show crenulation cleavage and thus this is not sketched further away fromt the shear zone. Away from the shear zone, C-S structures dominate (thin sections B, C, F, and G), while proximal to the shear zone (thin sections D and E), extensional shear planes C' developed at an angle to the shear zone foliation.

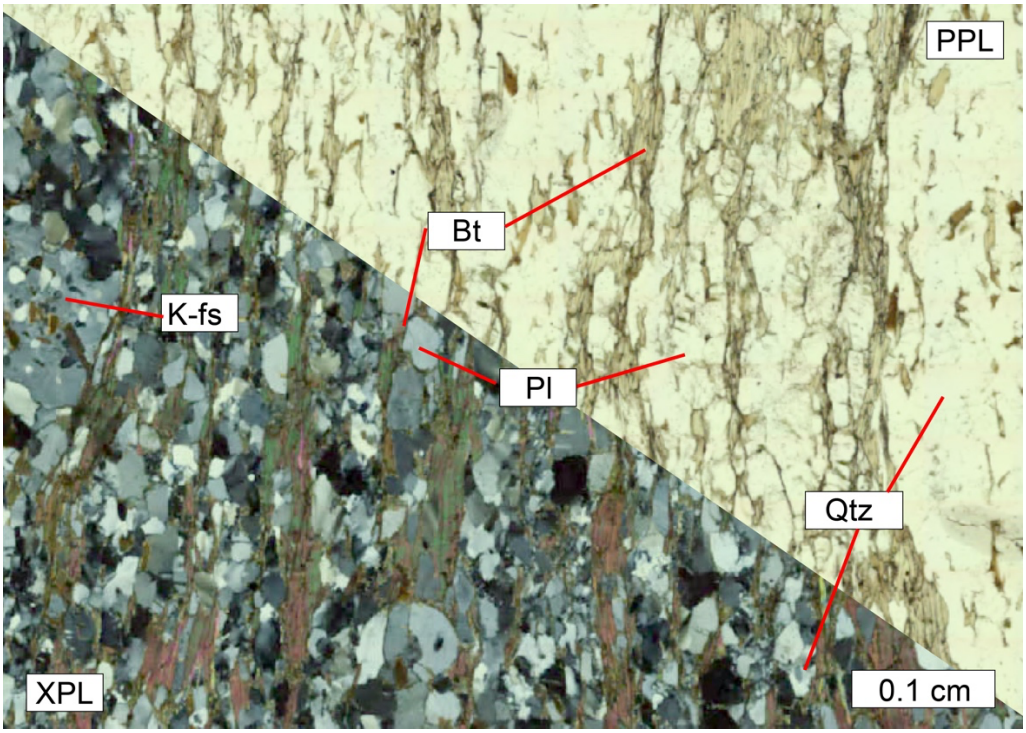

Figure 3.8: High resolution photograph of thin section C23-T1-A. K-fs=k-feldspar, Bt=biotite, Qtz=quartz, Pl=Plagioclase. This thin section also contained muscovite and sillimanite but not in the shown area. Foliation is mostly defined by biotite grains.

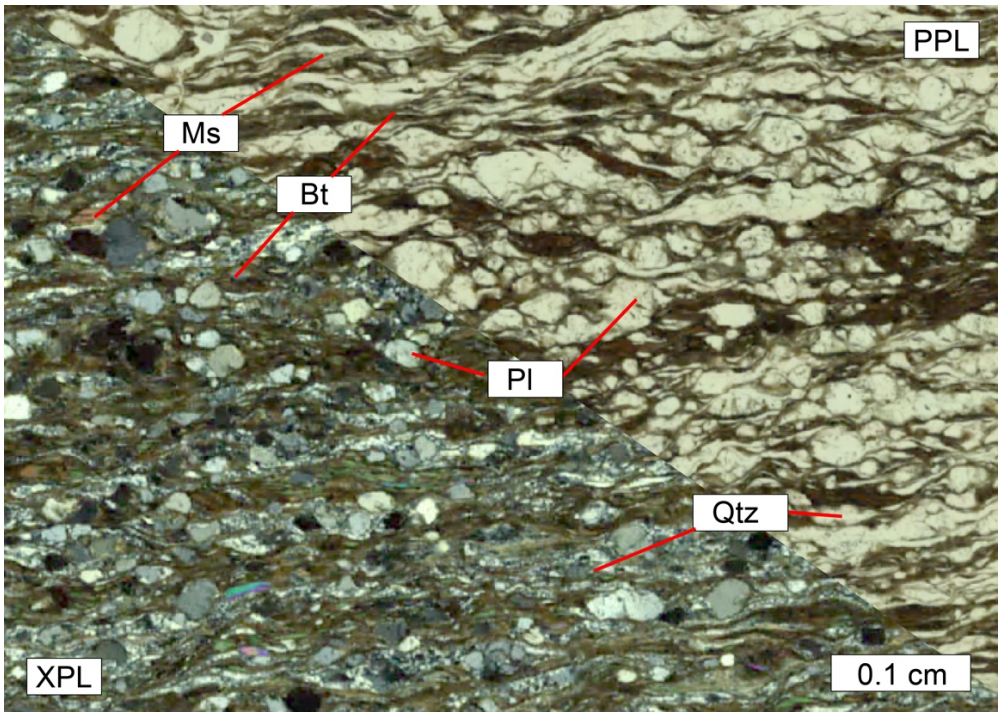

Figure 3.9: High resolution photograph of thin section C23-T1-E. Ms=muscovite, Bt=biotite, Qtz=quartz, Pl=plagioclase. Foliation is defined by biotite, muscovite and quartz. Almost all K-feldspar is gone

3.2 SEM and Automated mineralogy

Results section 3.2 contains SEM-scan results of the Cala Sardina en Tudela localities. These results consist of phase-color maps made by SEM and automated mineralogy and observations from these scans.

3.2.1 Cala Sardina

Thin section C23-S1-A

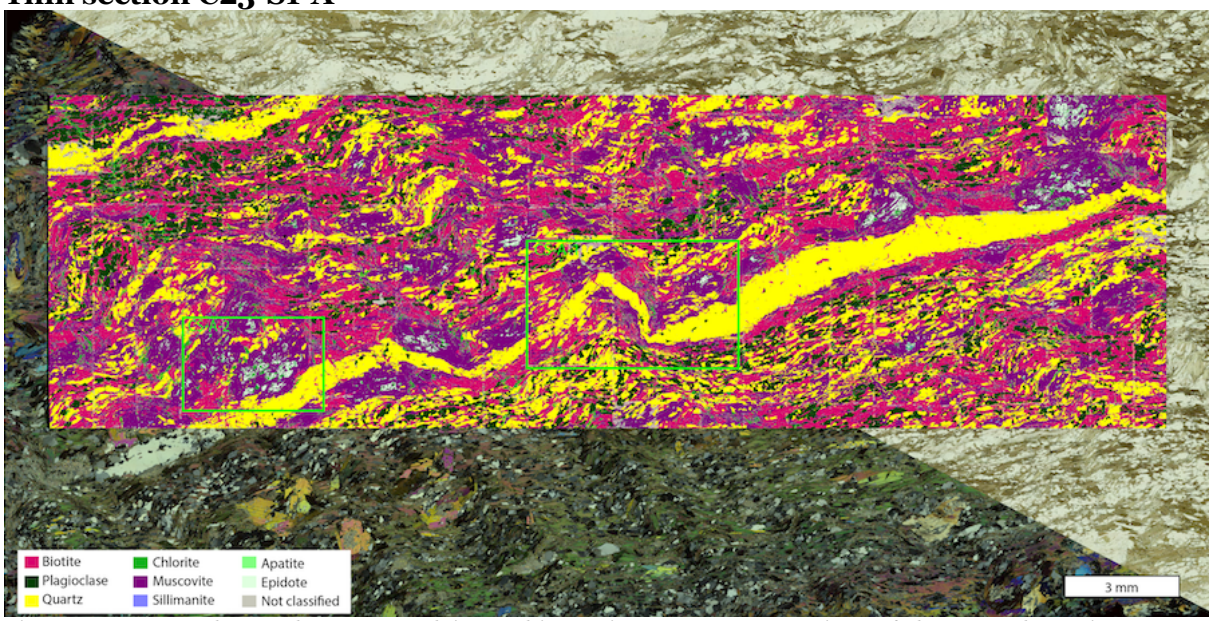

Figure 3.10: SEM phase-color map overlain on thin section C23-S1-A. Locations of close-ups shown in green. A larger image of this figure can be observed in Appendix I.

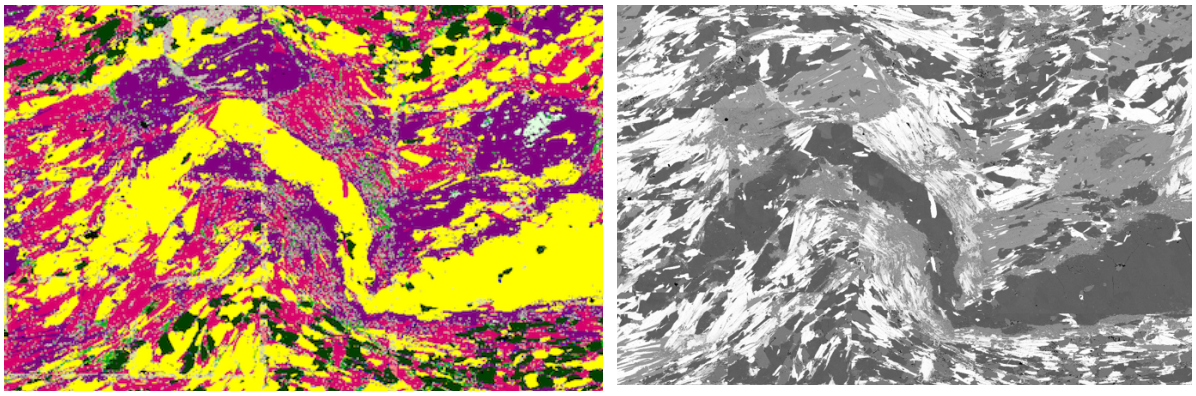

Figure 3.10.1: close-up CS-A-1

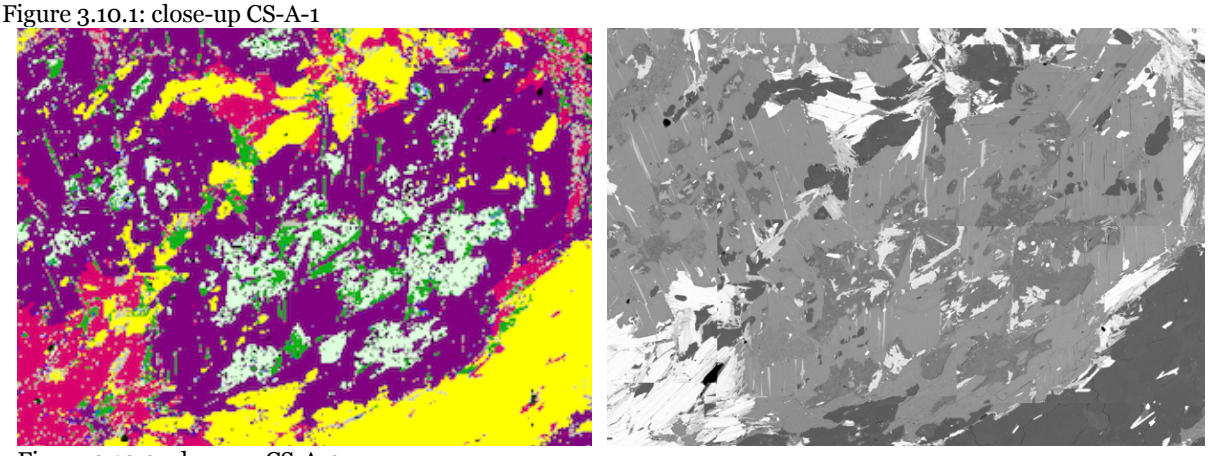

Figure 3.10.2: close-up CS-A-2

The minerals defining the dominant foliation and crenulation foliation visible in thin section C23-S1-A are quartz, biotite, plagioclase and muscovite, these minerals bend and show a deformed cleavage (fig. 3.10.1). The muscovite in nodules has straight cleavage planes and

appears undeformed, it grows over the quartz, biotite, muscovite and plagioclase grains, which in places also curve around the nodules (fig 3.10.1).

The nodules are formed by muscovite with epidote in their cores (fig. 3.10.1 and 3.10.2). This epidote has a chemical composition close to clinozoisite. The growth relation between the muscovite and epidote is unclear. The muscovite and epidote are overgrown by chlorite (fig. 3.10.2), which in turn is overgrown by a second low-Mg chlorite (fig. 3.10.2).

Thin section C23-S1-D

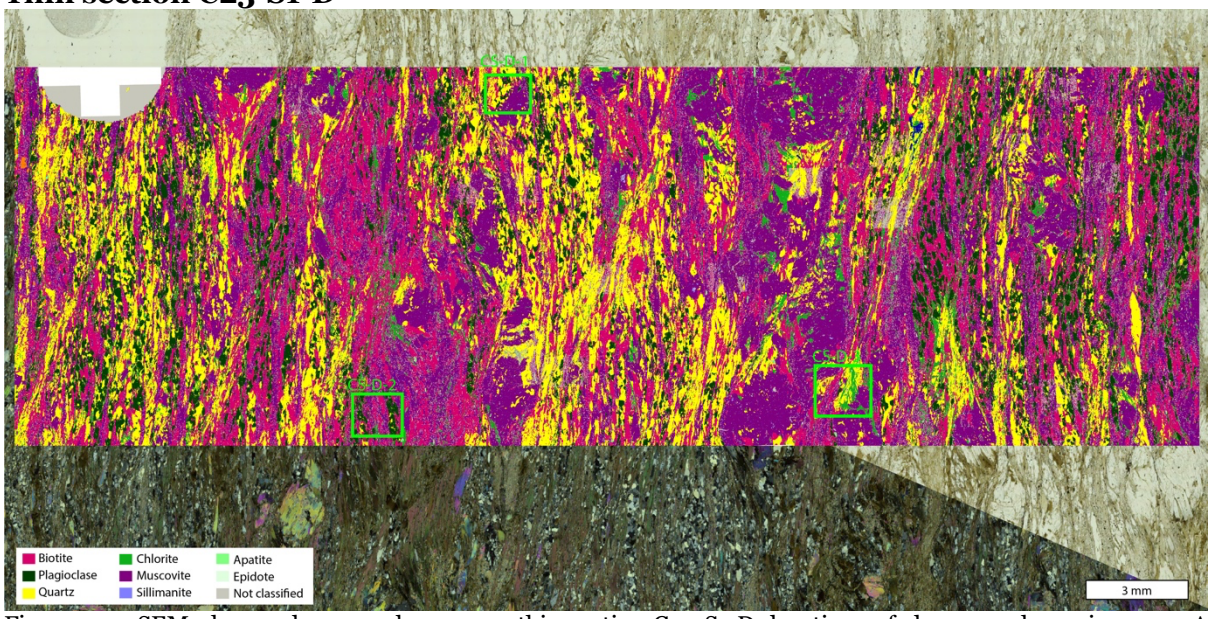

Figure 3.11: SEM phase-color map shown over thin section C23-S1-D, locations of close ups shown in green. A larger image of this figure can be observed in Appendix II.

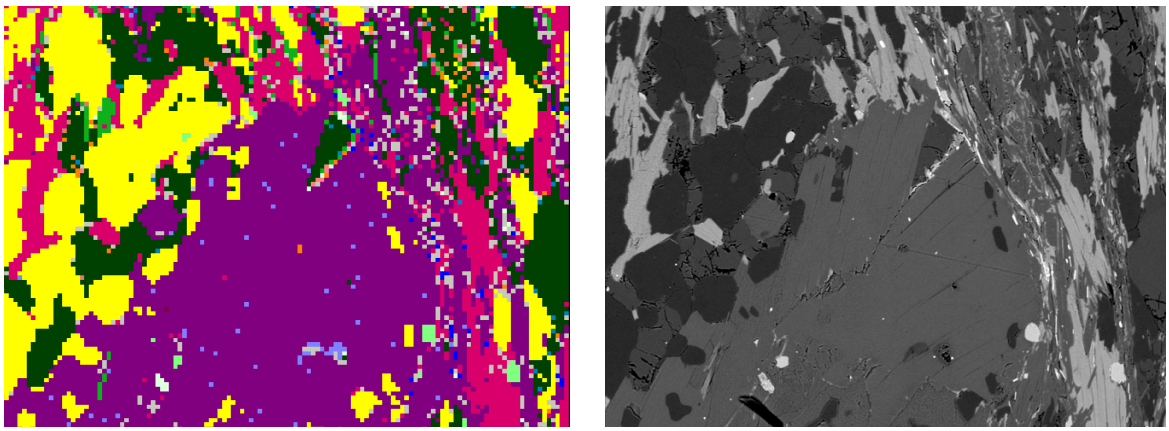

Fig. 3.11.1: Close-up CS-D-1

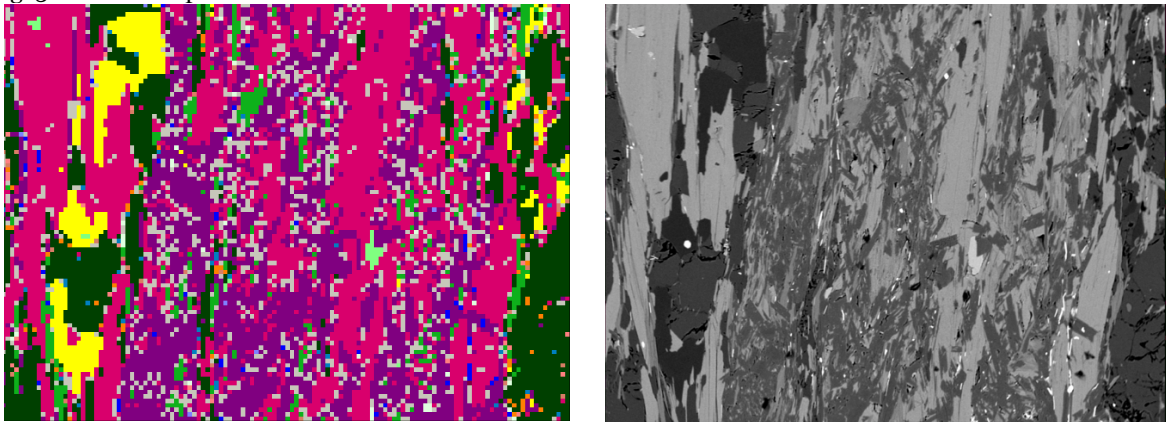

Fig. 3.11.2: Close-up CS-D-2

In this section C23-S1-D the previously observed matrix of biotite, muscovite, quartz and plagioclase is still defining the most prominent foliation, while the crenulation foliation makes a 20 degree angle with the dominant foliation. The grains of the matrix are more deformed (fig. 3.11.2) and observed to bend around the muscovite nodules (fig. 3.11.1). The muscovite in the nodules is much less deformed compared to the surrounding matrix, but does show some cracks and a minor bending of the cleavage in places (fig. 3.11.1). The epidote observed in the nodule-cores in C23-S1-A is also present but in much smaller quantities (fig. 3.11.1). Small muscovite grains are growing over the bended matrix biotite grains. These small muscovite grains are oriented at an angle to the dominant foliation (fig 3.11.2).

Chlorite is observed overgrowing muscovite nodules as in thin section C23-S1-A, but no low-Mg chlorite is observed. A later generation of quartz is overgrowing all other minerals, including the muscovite nodules and chlorite (fig. 3.11.1).

3.2.2 Tudela

Thin section C23-T1-A

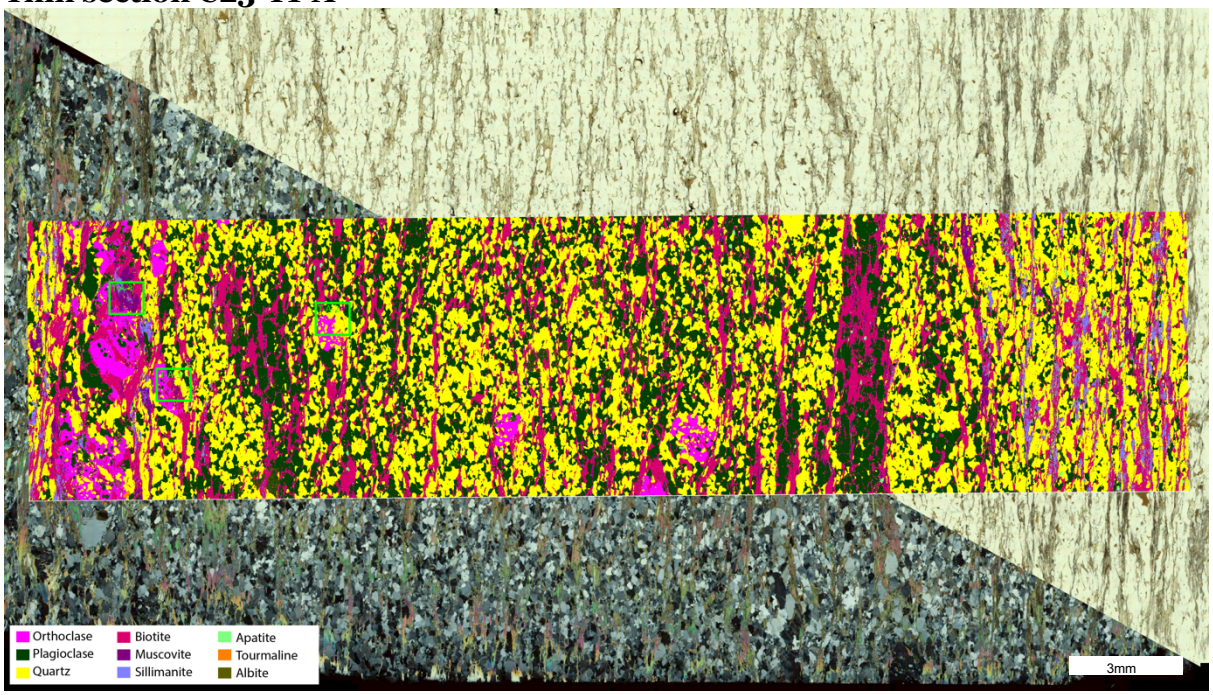

Figure 3.12: SEM phase color map over thin section C23-T1-A, locations of close ups in green. Larger image of this figure can be observed in Appendix III.

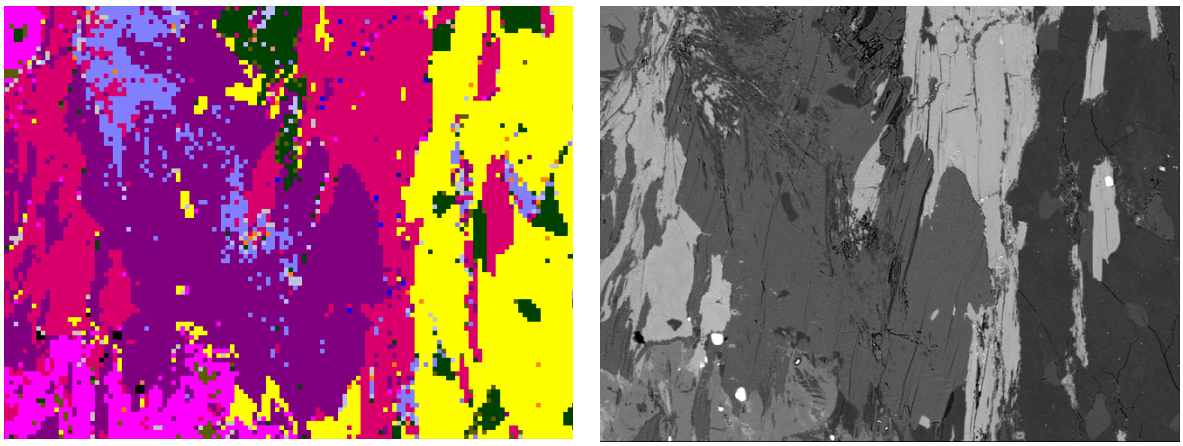

Figure 3.12.1: Close-up T-A-1

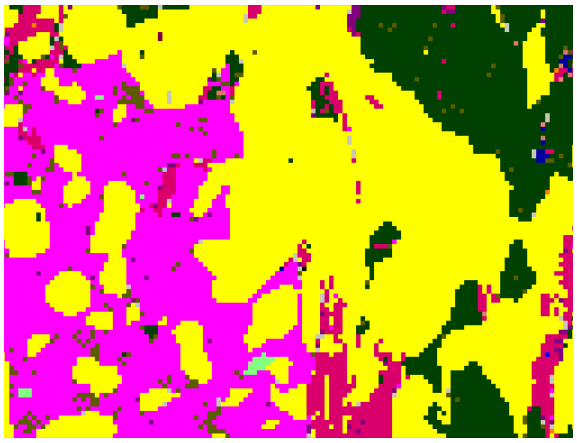
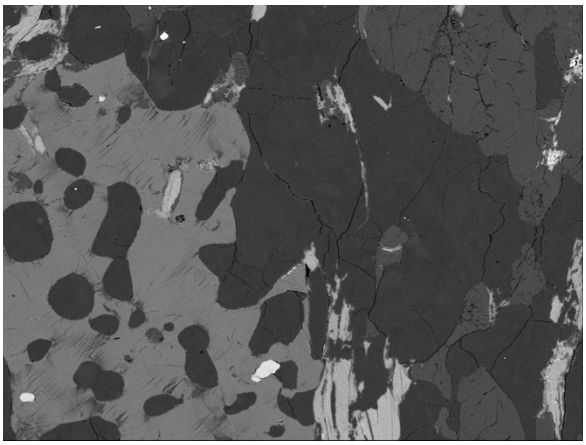

Figure 3.12.2: Close-up T-A-2

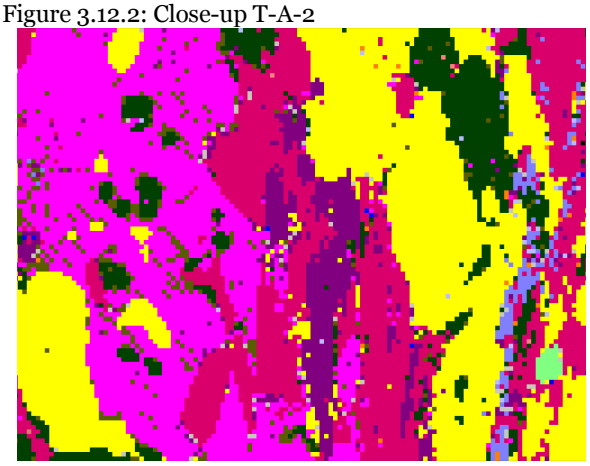
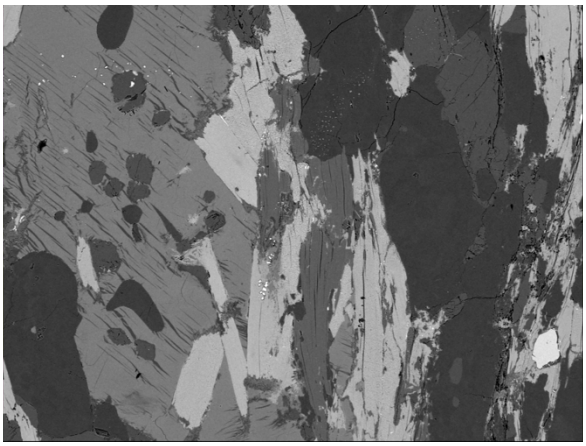

Figure 3.12.3: Close-up T-A-3

SEM images of C23-T1-A reveal a matrix of quartz, plagioclase and biotite, with the latter mostly defining the prominent foliation. Some areas of the section contain muscovite and sillimanite needles, both growing over the biotite (fig. 3.12.1). Muscovite is often also aligned with the dominant foliation direction. The thin section also contains K-feldspar blasts with albite exsolution lamellae (fig. 3.12.2 and 3.12.3) which are being overgrown by biotite and plagioclase first, later also quartz (fig. 3.12.2). The temporal relation between these blasts and matrix is difficult to determine due to new mineral growth, however in close up 3.12.1 the K-feldspar appears to grow over the muscovite.

Thin section C23-T1-I

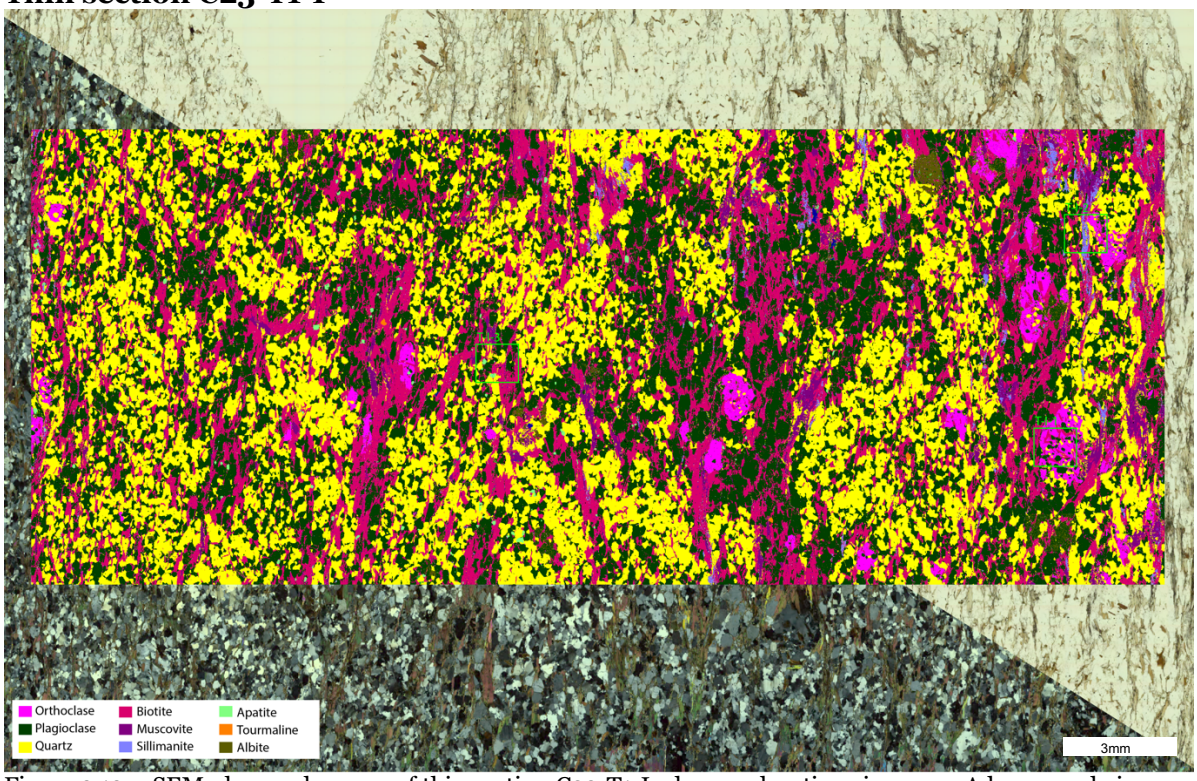

Figure 3.13: : SEM phase color map of thin section C23-T1-I, close-up locations in green. A larger scale image of this figure can be observed in Appendix IV.

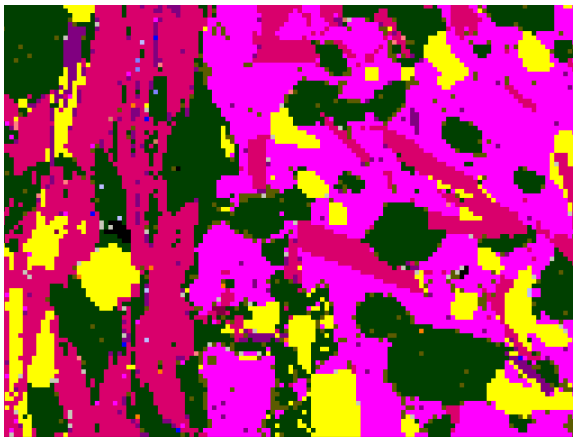

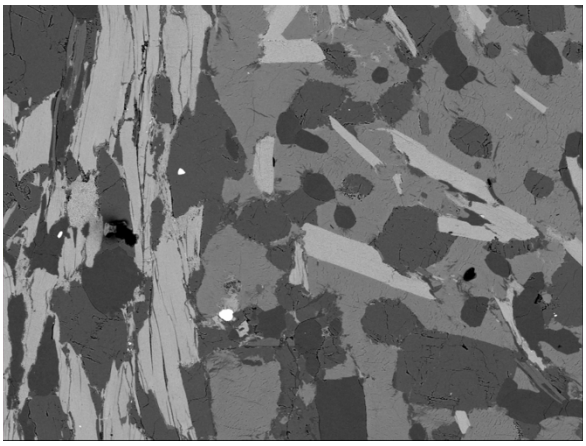

Figure 3.13.1: Close-up T-I-1

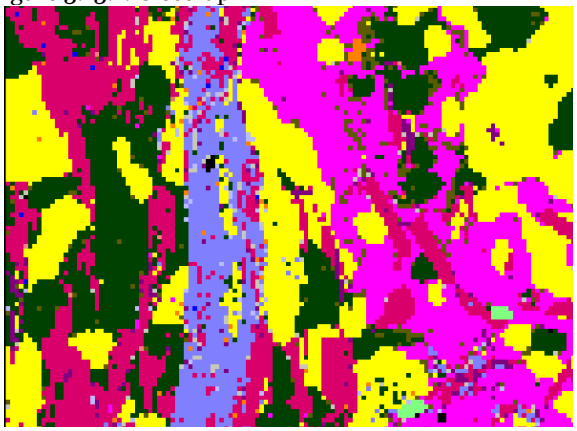

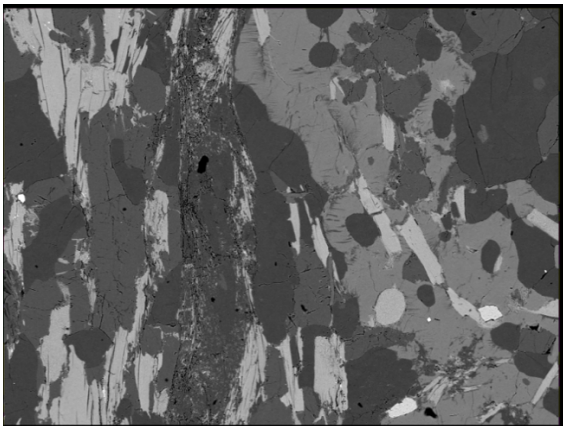

Figure 3.13.2: Close-up T-I-2

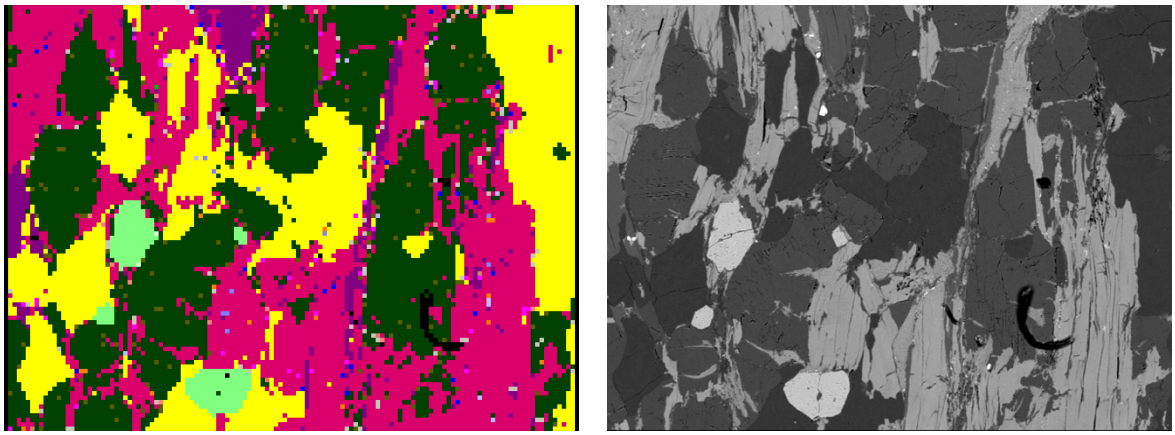

Figure 3.13.3: Close-up T-I-3

SEM images of thin section C23-T1-I show the same basic microstructures as observed in C23-T1-A but with more K-feldspar clusters. This K-feldspar is being overgrown by biotite, plagioclase and quartz (fig. 3.13.2 and 3.13.3). Biotite grains growing over the K-feldspar blasts are aligned with each other but not with the foliation observed in the thin section. Sillimanite and muscovite are again often observed to be overgrowing biotite (fig. 3.13.2, 3.13.3). Biotite can be observed bending around K-feldspar blasts (3.13.1). One albite grain is observed overgrowing all previous minerals except for quartz (fig 3.13 top right corner of BSE image).

Thin section C23-T1-E

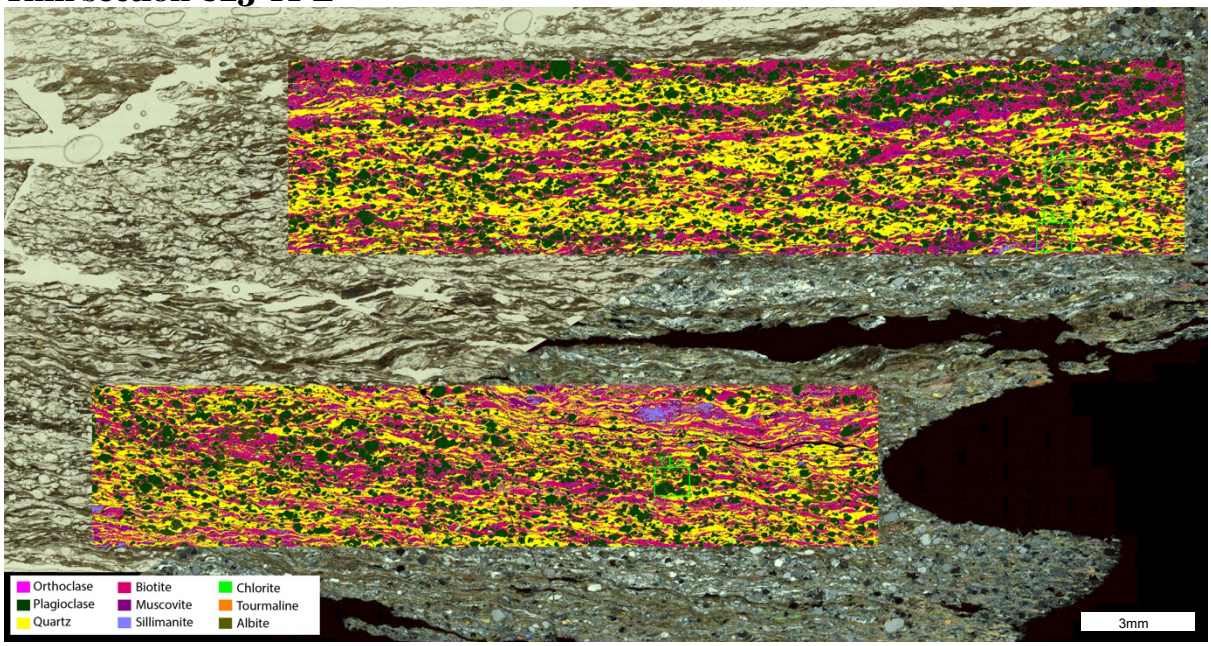

Figure 3.14: SEM-phase color maps of thin section C23-T1-E. Close-ups in green. A larger scale image of this figure can be observed in Appendix V.

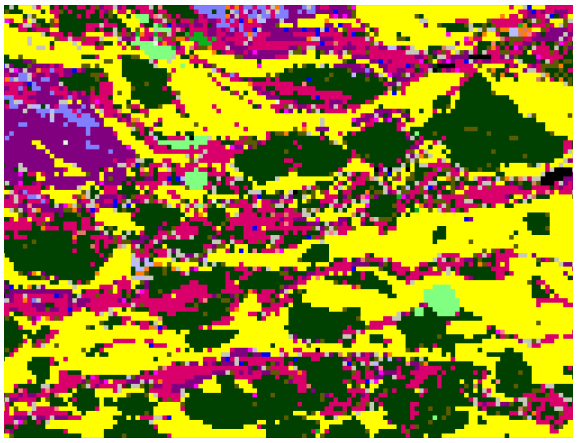
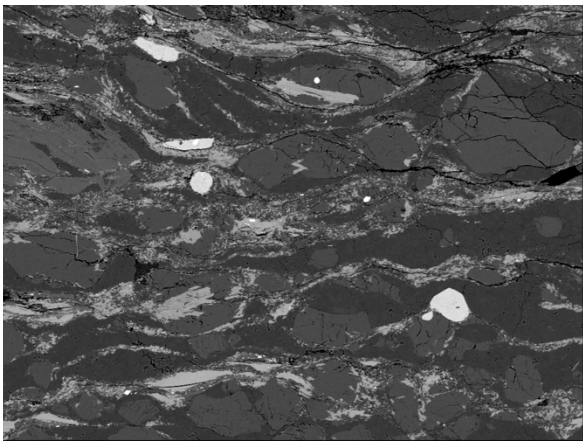

Figure 3.14.1: Close-up T-E-1

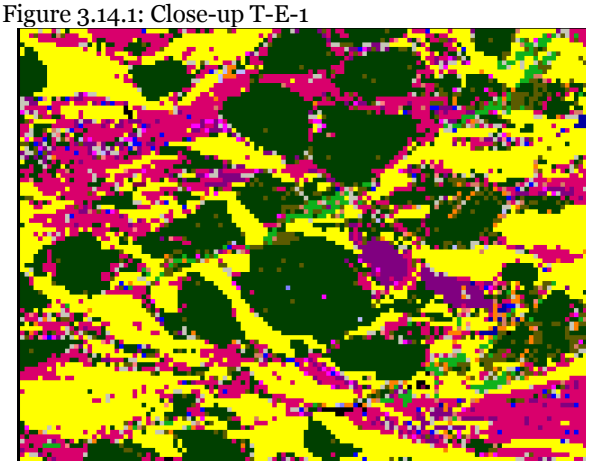
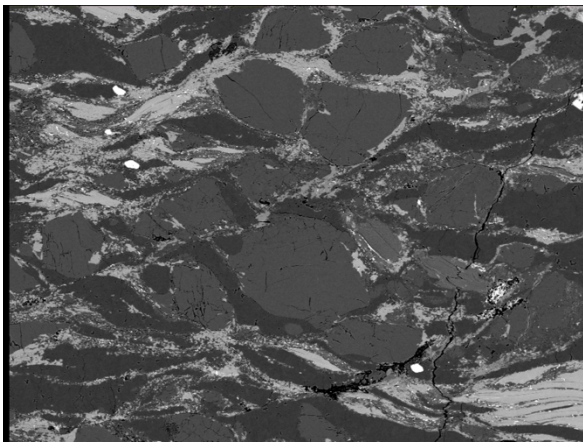

Figure 3.14.2: Close-up T-E-2

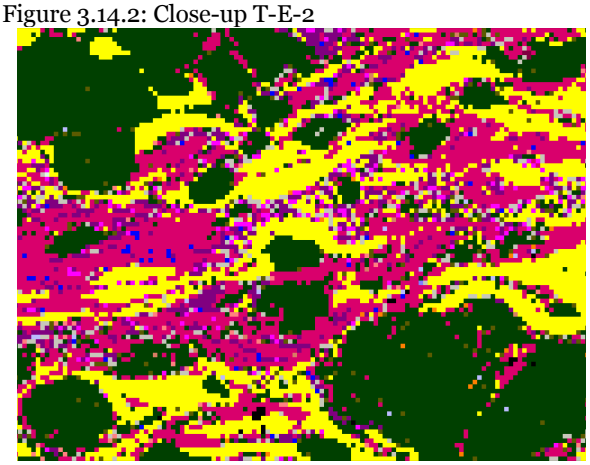
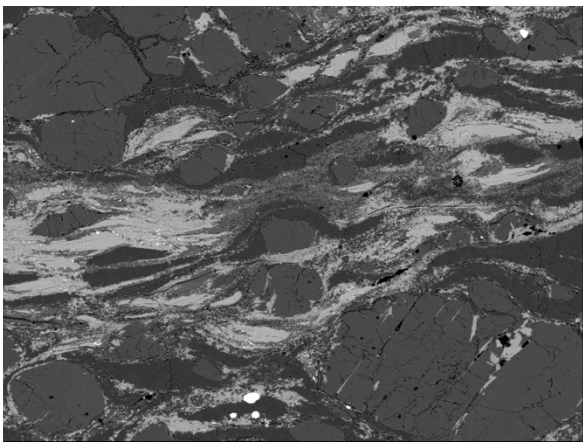

Figure 3.14.3: Close-up T-E-3

In the thin section C23-T1-E quartz, biotite, muscovite and sillimanite are deformed by a prominent crenulation foliation and bend around larger spherical plagioclase grains (fig. 3.14.3). In some cases biotite overgrows these plagioclase grains (fig. 3.14.1 and 3.14.3).
Sillimanite overgrows quartz and muscovite and follows the prominent foliation direction (fig. 3.14.1).
Very little chlorite is found in this thin section, mostly appearing along cracks and micro-shear zones in the sample (fig. 3.14.2).

3.3 Bulk rock composition

The following section of results describes the findings from bulk rock analysis applied to the samples from the Tudela and Cala Sardina localities. This consists of bulk rock compositions (from XRF-analysis and SEM-scans) and mineral proportion (calculated from SEM-scans).

3.3.1 Differences between XRF and SEM-AM

Both XRF-analysis and the EDS+AM-workflow were used to determine the bulk rock composition of the samples. All samples were analyzed with the XRF while only selected samples were analyzed with both XRF and AM techniques.
For the Cala Sardina samples, C23-S1-A and C23-S1-D were analyzed using both methods. For major oxides the BRC differences between the XRF and SEM-AM-analysis were within 10% of the concentration. The BRC from EDS+AM analysis and XRF analysis for sample C23-S1-A are very similar but show a larger difference for sample C23-S1-D.
For the Tudela section the samples C23-T1-A, C23-T1-E and C23-T1-I were analyzed with both methods. The difference in concentration between XRF and EDS+AM are higher in these samples; up to 20% for the major oxides.
These differences may affect the resulting psuedosections for these samples, and will be further addressed in the discussion.

3.3.2 Cala Sardina

Bulk rock composition Cala Sardina

	C23-S1-A		C23-S1-B	C23-S1-C	C23-S1-D	
	EDS+AM	XRF	XRF	XRF	EDS+AM	XRF
SiO2	56.2	53.5	54.8	55.9	53.0	51.4
Al2O3	20.6	19.6	19.1	18.6	22.4	20.7
Fe2O3	9.89	9.30	8.85	8.71	10.2	9.48
MgO	4.23	4.37	4.15	4.07	4.54	4.52
CaO	0.94	1.00	0.94	0.85	1.20	0.80
Na2O	1.20	1.30	1.23	1.16	1.23	1.10
K2O	5.72	5.46	5.40	5.27	6.11	6.06
TiO2	1.04	0.77	0.76	0.75	1.09	0.83
MnO	0.08	0.12	0.11	0.11	0.09	0.12

Table 3.4: Bulk rock composition of Cala Sardina samples in oxide-weight percentage

The variations in oxides for all samples are small, under 10% diff in wt% for all major oxides, and no clear trends can be found with distance from the Cala Sardina shear zone.

Mineral proportions

	Bt	Qz	Ms	Pl	Chl	Ilm	Ep	Ab	Tour
C23-S1-A	29.7	23.0	23.8	11.0	3.34	0.65	0.63	0.19	1.37
C23-S1-D	27.1	17.2	27.6	11.4	5.91	0.79	0.72	0.3	0.71

Table 3.5: Mineral proportions of samples C23-S1-A and C23-S1-D, for the 8 minerals with the highest concentrations all given in weight percentages.

For the samples C23-S1-A and C23-S1-D the automated mineralogy results were used to obtain mineral proportions. From sample S1-A to sample S1-D (i.e. with proximity to the shear zone) there is a notable increase in muscovite, chlorite and albite and there is a decrease in biotite

and quartz. The increase in muscovite and chlorite is also qualitatively visible in the ppl thin section and SEM false-color maps (fig. 3.7 and 3.8).

3.3.3. Tudela

Bulk rock composition Tudela

	C23-T1-A		C23-T1-B	C23-T1-C	C23-T1-D	C23-T1-E	
	EDS+AM	XRF	XRF	XRF	XRF	EDS+AM red	XRF
SiO2	70.5	67.9	67.6	67.2	67.2	68.4	65.3
Al2O3	15.4	14.8	14.8	15.0	15.0	16.9	15.7
Fe2O3	4.76	4.92	4.95	4.96	5.11	4.89	5.36
MgO	1.83	2.06	2.04	2.05	2.09	1.81	2.19
CaO	1.60	1.54	1.68	1.58	1.48	1.59	1.49
Na2O	3.04	2.61	2.84	2.67	2.55	3.16	2.57
K2O	2.67	2.70	2.65	2.92	2.85	2.77	2.95
TiO2	0.18	0.61	0.62	0.63	0.64	0.50	0.69
MnO	0.0015	0.06	0.06	0.05	0.05	0.00078	0.06

	C23-T1-I		C23-T1-H	C23-T1-G	C23-T1-F	C23-T1-E	
	EDS+AM	XRF	XRF	XRF	XRF	EDS+AM green	XRF
SiO2	67.1	67.9	66.7	68.2	65.4	67.5	65.3
Al2O3	16.5	14.6	15.3	14.6	15.7	16.9	15.7
Fe2O3	5.55	4.84	5.28	4.49	5.43	5.01	5.36
MgO	2.17	1.99	2.15	1.84	2.21	1.9	2.19
CaO	1.82	1.69	1.66	1.91	1.56	1.9	1.49
Na2O	3.52	2.91	2.77	3.02	2.52	3.43	2.57
K2O	3.01	2.83	3.02	2.57	3.39	2.69	2.95
TiO2	0.2	0.63	0.69	0.61	0.7	0.6	0.69
MnO	0.0015	0.0596	0.06	0.05	0.06	0.0019	0.06

Table 3.6: Bulk rock composition of Tudela samples in oxide weight percentages.

For the Tudela samples two distinct layers were analyzed. Most proximal to the shear zone these two layer are both present in sample C23-T1-E which makes the BRC calculated with the XRF a mixed composition of both layers for this sample.
No large differences in major oxides are found, all around 5% variations in wt%. No clear trend in oxide variations is found neither.

Mineral proportions

	Qz	Pl	Bt	Ms	Kfs	Ab	Sill	Ilm	Tour
C23-T1-A red	38.1	29.5	21.8	2.73	2.45	1.52	1.63	0.26	0.34
C23-T1-E red	30.9	27.8	23.9	6.76	0.97	3.33	0.62	0.71	0.64
C23-T1-I green	30.9	34.0	25.4	3.02	2.06	2.11	0.72	0.26	0.2
C23-T1-E green	30.1	31.3	23.4	6.11	0.55	3.13	0.21	0.90	0.54

Table 3.7: Mineral proportions for samples C23-T1-A to C23-T1-E and C23-T1-I to C23-T1-I all given in weight percentages.

From sample C23-T1-A to C23-T1-E there is a decrease in quartz, plagioclase, K-feldspar and sillimanite and an increase in biotite, muscovite and albite.
From samples C23-T1-I to C23-T1-E there is a decrease in quartz (very minor), plagioclase, biotite, K-feldspar and sillimanite and an increase in muscovite and albite.

3.4 Thermodynamic modelling

Section 3.4 contains the results of thermodynamic modelling in Perple_X for selected samples. This consist of psuedosections for both the Tudela and Cala Sardina localities.

3.4.1 Parameters: Fe-ratio and water content

For the thermodynamic modelling two parameters needed to be determined; the Fe-oxide ratio and the water content present during deformation.
Fe-oxide ratio ($X_{Fe^{3+}}$) is the ratio of FeO to Fe2O3 present, where $X_{Fe^{3+}} = Fe^{3+}/(Fe^{2+} + Fe^{3+})$. The two BRC analyses performed in this research both output a sum of FeO and Fe2O3 together, thus no ratio could be deduced from this. The paper of Forshaw and Pattison (2021) shows that the presence of ilmenite (table 3.5 and 3.7) makes X=0.2±0.09 the most likely ratio for all samples in this research. Different model runs with X=0.11, X=0.2 and X=0.29, to cover the end-members and mean, was performed for both localities.

Multiple model runs with different water content were made; saturated (all possible water needed in phase reactions is available), 5 wt% H2O, 2 wt% H2O and 1 wt% H2O. Differences between these plots were noted and compared with the mineral assemblage observed in samples.

3.4.2 Cala Sardina

Psuedosections for the different bulk rock composition of the Cala Sardina samples are modelled over a pressure range of 1-5 kbar and a temperature range of 573°-973° K.

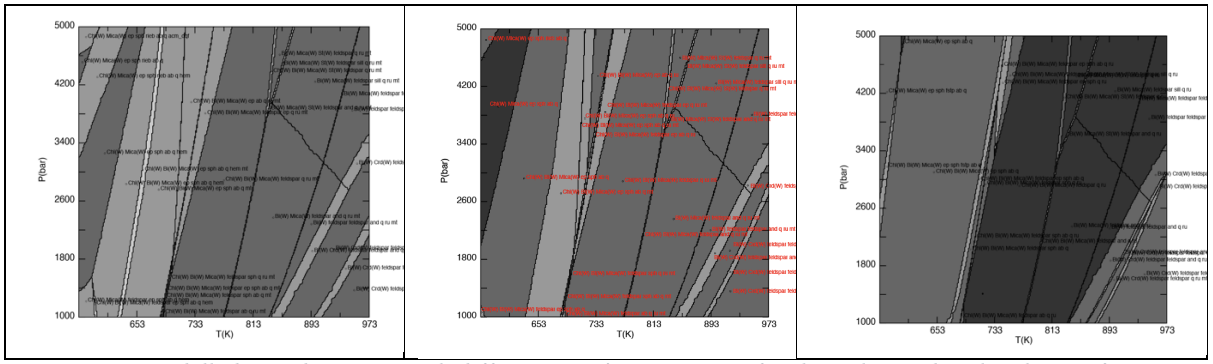

Figure 3.15: Modelled psuedosection with different FeO/Fe2O3 ratios for the Cala Sardina locality. Left: x=0.29, middle: x=0.2, right: x=0.11.

Modelling different FeO/Fe2O3 ratios for the Cala Sardina locality shows some differences in the phase reactions possible/present in the system. Both the models for x=0.29 and x=0.11 mainly show differences with x=0.2 at lower temperatures for the plagioclase-feldspar phase reactions. At higher temperatures the stability fields for all models are very similar. As x=0.20 is the average ratio and not many notable differences are observed (for stability fields that match the mineral assemblage of the samples from this locality) at lower or higher ratios, this ratio is taken for the Cala Sardina locality.

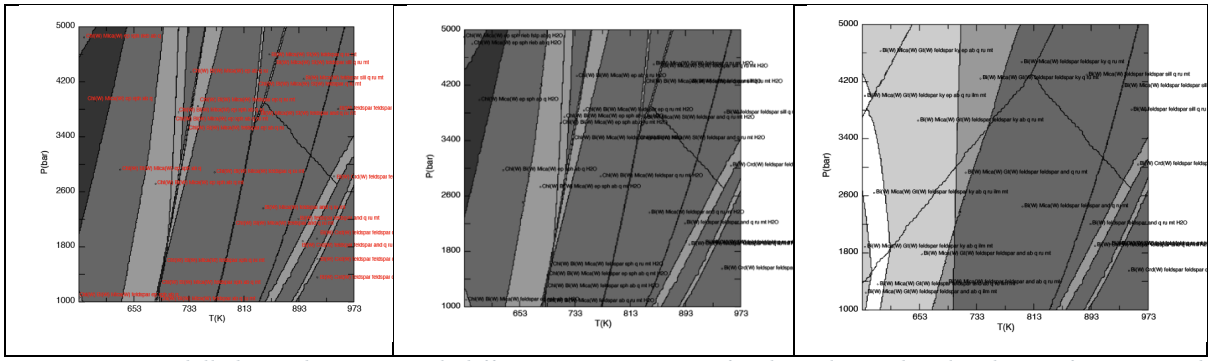

Figure 3.16: Modelled psuedosection with different water contents for the Cala Sardina locality. Left: Saturated, middle: 5 wt% water, right: 2 wt% water.

Water-content modelling shows that 5 wt% H2O does not alter the modelled psuedosections compared to saturated modelling, thus at 5 wt% H2O the system is still saturated. At 2 wt% H2O there is a shift in many of the phase-reactions present in the model, thus the system is undersaturated in H2O. A shift in the ky-and-sill field allows for andalusite at much lower PT conditions and a change in the K-feldspar reactions allows it to grow at lower temperatures. Most notably in the undersaturated model there is no possibility for chlorite to form. As there is an amount of chlorite present in our thin sections this undersaturated model is unlikely.

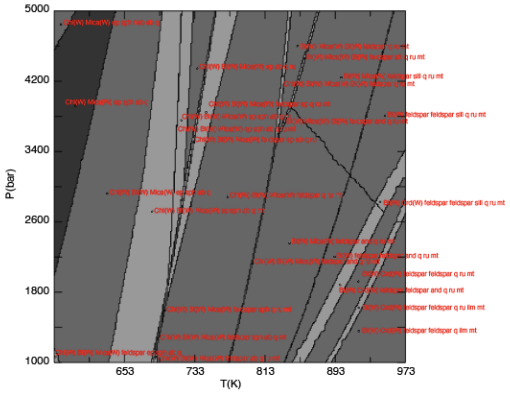

A: C23-S1-A SEM+AM-BRC

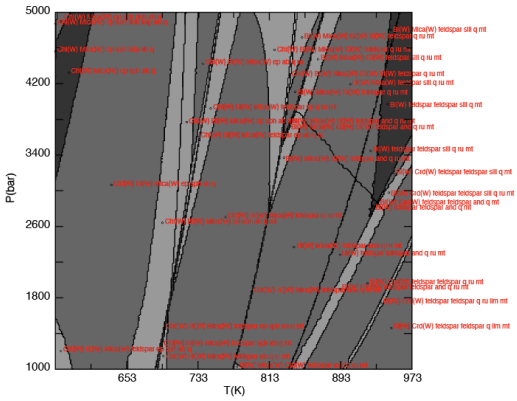

B: C23-S1-A XRF-BRC

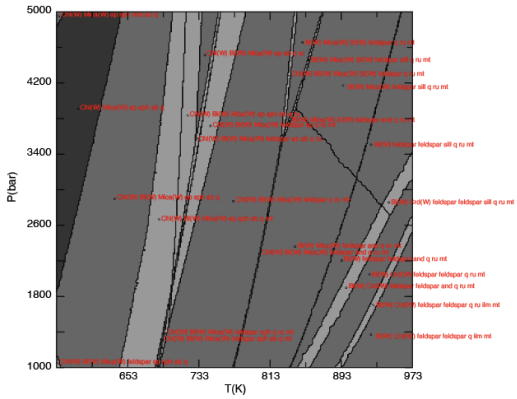

C: C23-S1-D SEM+AM-BRC

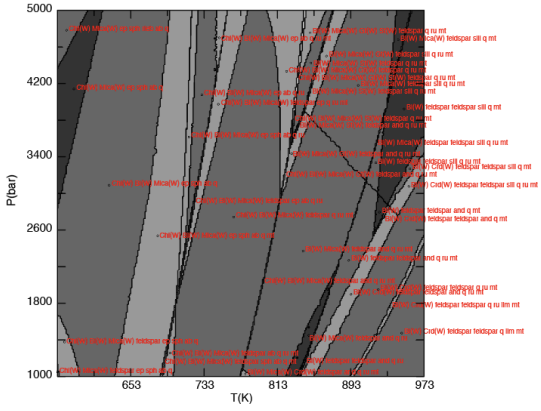

D: C23-S1-D XRF-BRC

Figure 3.17: Psuedosections for BRC of samples C23-S1-A and C23-S1-D, X_(〖Fe〗^(3+))=0.2, H2O is saturated. A=C23-S1-A with SEM+AM calculated BRC, B=C23-S1-A with XRF-calculated BRC, C=C23-S1-D with SEM+AM calculated BRC, D=C23-S1-D with XRF-calculated BRC.

Model results with H2O saturation and X=0.2 are shown in figure 3.17. When all the different BRC compositions obtained for the Cala Sardina locality are modelled not many large differences exist between the psuedosections, as expected, as all BRC's were very similar. It is noted that there is especially a strong similarity between the BRC models obtained with the same technique (SEM-AM: fig 3.12 A and C, XRF: fig. 3.12 B and D). There are however some minor differences between the SEM-AM and XRF pseudosections, most notably as the latter contains stability fields for garnet, which is not modelled for the SEM-AM BRC. For the discussion both the psuedosection modelled with SEM-AM-BRC and XRF-BRC for section C23-S1-A will be addressed.

3.4.3 Tudela

Psuedosections for the different bulk rock composition of the Cala Sardina samples are modelled over a pressure range of 1-5 kbar and a temperature range of 573°-973° K.

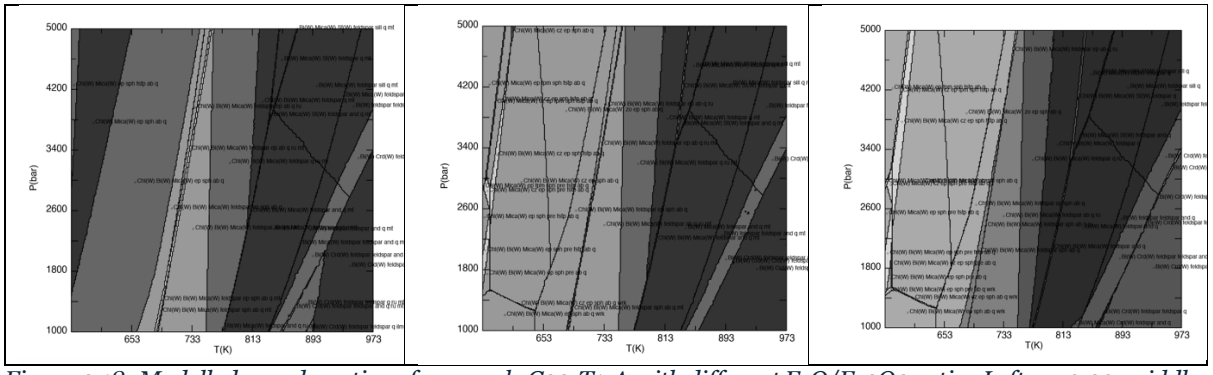

Figure 3.18: Modelled psuedosections for sample C23-T1-A with different FeO/Fe2O3 ratio. Left: x=0.29, middle: x=0.20, right: x=0.11.

Varying the FeO/Fe2O3 ratio for the thermodynamic models for the Tudela samples shows mainly differences at lower temperatures for the feldspar stability fields (as is also observed for the Cala Sardina samples). As these phase reactions are not very important for our research, and to remain consistent with respect to the Cala Sardina results, the average ratio of x=0.20 is taken for the Tudela samples as well.

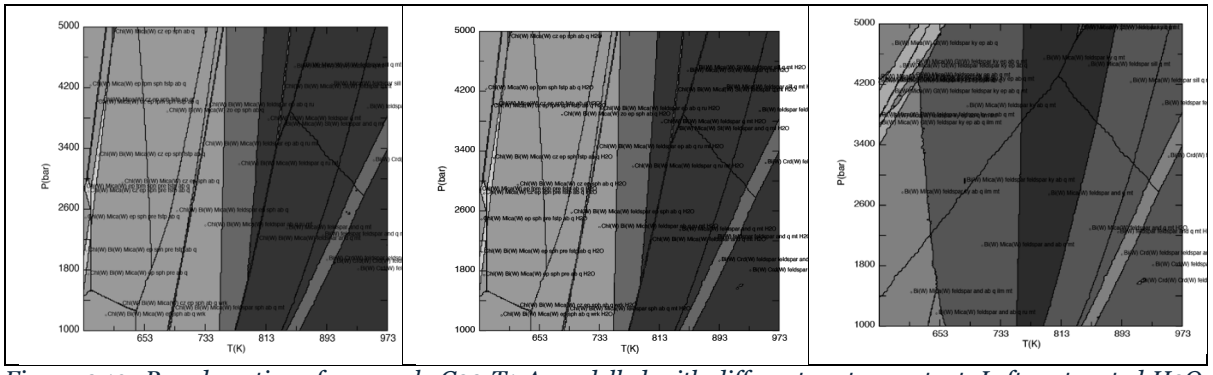

Figure 3.19: Psuedosections for sample C23-T1-A modelled with different water content. Left: saturated H2O, middle: 5 wt% H2O, right: 1 wt% H2O.

For the Tudela samples the modelled psuedosection with saturated water content and 5 wt% water content are the same, showing that the Tudela locality system is still saturated at 5 wt% H2O. At 1 wt% H2O the modelled stability fields change, most notably for chlorite which is no longer stable. As there are only traces of chlorite in this thin section, and only along cracks (fig. 3.11.2), it is possible that the Tudela locality was undersaturated during all deformation events, or that deformation temperatures were too high for chlorite to form. This observation will be expanded on in the Discussion section.

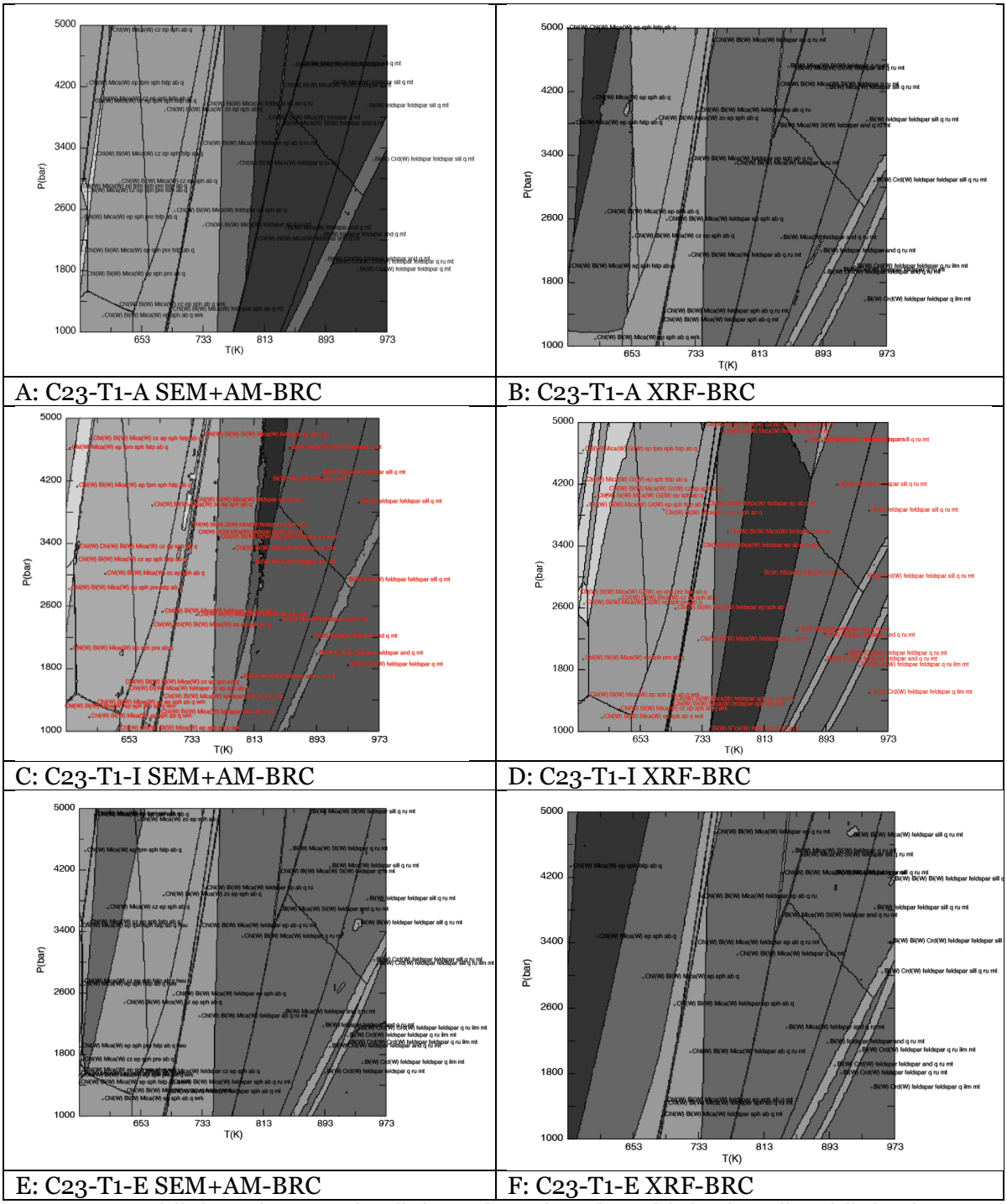

Figure 3.20: Modelled psuedosections for all obtained BRC from the Tudela locality, all modelled with saturated H2O and X=0.20.

Model results with H2O saturation and X=0.2 are shown in figure 4.20. As with the Cala Sardina pseudosections, the modelled sections for Tudela show strong similarities between the same technique (SEM-AM: A, C, E. XRF: B, D, F), while some differences can be observed between techniques. These differences appear larger compared to the results for Cala Sardina. This can be due to the samples coming from 2 different compositional layers, or due to different analytical techniques. In the Discussion section the pseudosections for sample C23-T1-A will be reviewed.

3.5 Minor, trace, and rare-earth elements

Section 3.5 of the results contains an analysis of the minor, trace, and rare-earth elements (as described in methods sections 2.5) for the Cala Sardina and Tudela localities based on Laser Ablation and XRF data.

3.5.1 Cala Sardina

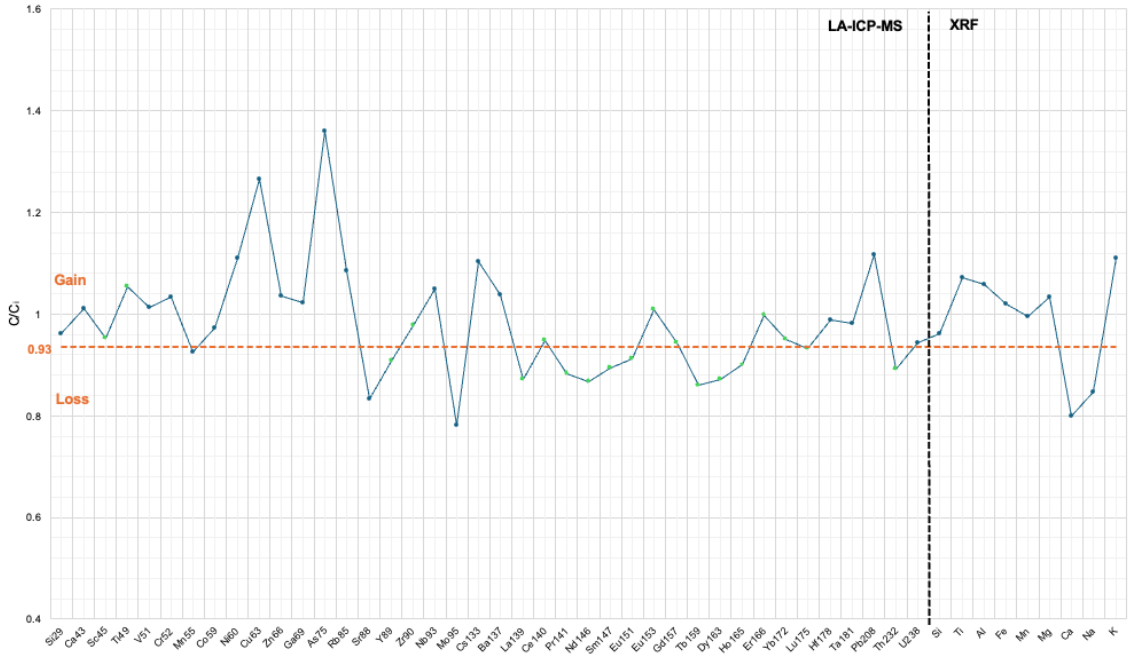

Figure 3.21: Concentration ratio diagram of sample C23-S1-D and sample C23-S1-A. Immobile elements annotated with green markers. Dashed orange line shows the average ratio of immobile elements.

For Cala Sardina the ratio C/Ci is calculated with LA-ICP-MS and XRF element concentrations from C23-S1-D (most proximal sample) for C, and C23-S1-A (most distal sample) for Ci. The average C/Ci ratio for all the immobile elements (HFSE (Zr, Hf, Nb, Ta, Ti, Th) and REE (Sc, Y, La-Lu)) combined is 0.93 (orange dashed line in graph 4.21). C/Ci values (plotted in graph 3.21) above 0.93 are considered a mass percentage gain, C/Ci values below this are considered mass percentage loss. Visible in fig. 3.21 the mass percentage gain goes up to a C/Ci ratio of 1.36, mass percentage loss reaches a C/Ci ratio of 0.78.
Using the inverse of the average C/Ci ratio of the immobile elements (as described in the methods section) gives us a total mass transport of +8.14% when comparing sample C23-S1-D to C23-S1-A.

3.5.2 Tudela

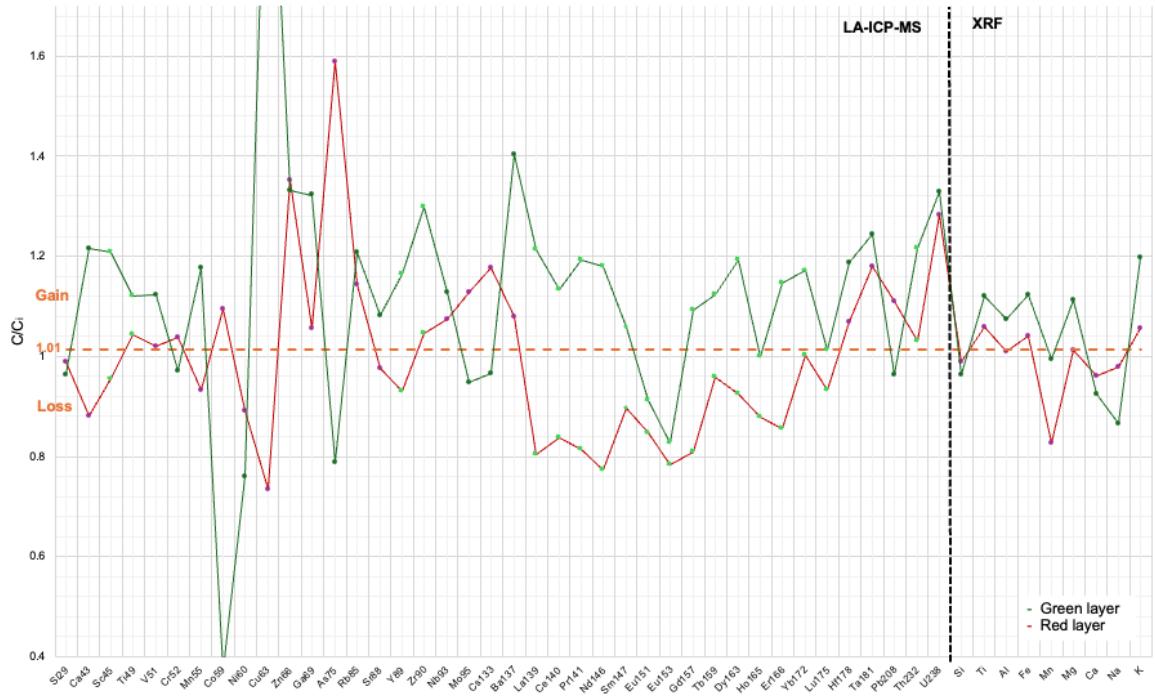

Figure 3.22: Concentration ratio diagram of sample C23-T1-F in respect to C23-T1-I ("green layer") and C23-T1-A in respect to C23-T1-D ("red layer"). Immobile elements annotated with green markers. Orange dashed line shows the average ratio of immobile elements.

For the Tudela green layer the ratio C/Ci is calculated with element concentrations from C23-T1-F for "altered composition" C and C23-T1-I for "initial composition" Ci. For the Tudela red layer the ratio is calculated with C23-T1-D concentrations for "altered composition" C and C23-T1-A for "initial composition" Ci. The average C/Ci ratio for the immobile elements (Zr, Ti, Th and REE) for both the red and green layer combined is 1.01, thus C/Ci values above this are considered as mass percentage gain, C/Ci values below this are considered mass percentage loss.
Visible in fig. 3.22 mass percentage gain goes up to C/Ci ratio of 2.69 while the lowest mass percentage loss is 0.44. This is a much wider spread than for the Cala Sardina samples.
For the green layer (C23-T1-F to C23-T1-I) a total mass change of -9.69% is calculated, for the red layer (C23-T1-A to C23-T1-D) a total mass change of +11.1% is calculated. The negative or positive value here refers to if mobile elements are removed or added to the rock, which is interestingly different for these two layers and will be addressed further in the discussion. The absolute mass that is moved (be it removed or added) is very similar for each layer.

4. Discussion

Cala Sardina summary of results

The Cala Sardina samples were taken from a migmatised sillimanite-schist layer dragged into a large scale shear zone with sample points spaced 10's of cm's apart, with a total distance of 88 cm sampled. Shear strain values ranged from 0.0 for the most distal sample to 3.2 for the most proximal sample.

In samples further away from the shear zone a matrix of Qz+Bi+Ms+Plag shows a dominant first foliation and a crenulation cleavage, these minerals show no clear timing relations. A later generation of Muscovite is found in Ms+Ep nodules, where epidote overgrows muscovite. These nodules show no obvious signs of deformation. All previous minerals are overgrown by two generations of chlorite, the latter being Mg-poor.
Closer to the shear zone the angle between the crenulation and dominant foliation becomes more acute, where the foliation is defined by the Qz+Bi+Ms+Plag matrix. A decrease of grain size for these minerals is observed compared to the distal sample. Muscovite nodules remain a similar size between distal and proximal samples, while the muscovite nodules do show minor signs of deformation in the more proximal samples.
In summary the temporal relation between the different minerals observed is as follows:
i) Qz+Bi+Ms+Plag matrix, ii) Muscovite+epidote nodules, iii) chlorite, iv) Mg-poor chlorite. Interestingly the matrix is observed to be bending around the Ms-nodules, but the nodules do not show signs of deformation in samples distal to the shear zone and are only minorly deformed proximal to the shear zone.

Bulk rock composition analysis of all Cala Sardina samples shows no major changes in oxide weight percentage over the sampled distance. When comparing C23-S1-A (distal to shear zone) to C23-S1-D (proximal to shear zone) mineral changes show a decrease in biotite and quartz and an increase in muscovite, plagioclase and chlorite. Thermodynamic modelling of the found bulk rock composition reveals the rock was likely water saturated during deformation. Analysis of the minor, trace and RE-elements reveals a mass transfer of these elements comparing proximal to distal samples due to water transport. A total mass transfer of +8.14% in mobile elements is calculated for the proximal sample C23-S1-D compared to the "unaltered" distal sample C23-S1-A.

Tudela summary of results

The Tudela samples were taken from two lithological layers of the sillimanite-K-feldspar zone in Cap de Creus. These two layers were adjacent and deformed by the same smaller scale shear zone, from which samples were taken cm's apart, with a total distance of 20 cm sampled. Shear strain values range from 0.7 for the samples furthest from the shear zone and 114.1 closest to the shear zone.

Both sampled layers show the following mineral growth;
The samples furthest from the shear zone consist of a Pl+Q+Bi matrix defining a dominant foliation. The biotite grains in the matrix are often overgrown with muscovite and sillimanite (sillimanite growing in needles over the biotite and muscovite). K-feldspar-blasts grow over this matrix, the grains in the matrix are observed bending around these blasts. The K-feldspar has exsolution lamellae and the blasts are overgrown by plagioclase and biotite first, later also by quartz. The biotite grains overgrowing the K-feldspar blasts are not aligning with the dominant foliation. Albite is observed overgrowing the older and newer generation of plagioclase in these samples. The resulting temporal relations between the minerals resulting from these observations is as follows: i) the matrix of biotite, plagioclase and quartz forms, which is ii) overgrown by muscovite and sillimanite needles. Subsequently, iii) the K-feldspar blasts grow, which are in turn iv) overgrown by a second generation of biotite and plagioclase, and lastly v) quartz and albite.

Closer to the shear zone the prominent foliation observed is paired with a crenulation foliation and average grain size of biotite and quartz decreases. Small quartz, biotite and muscovite grains bend around spherical plagioclase grains, which remain a relatively larger size. The clusters of K-feldspar disappear completely and sillimanite is rarely observed. Very little chlorite is found, mostly along cracks in the rock.

Bulk rock composition data for both layers analyzed shows no clear trend from distal to proximal samples. The mineral content of the first analyzed layer (C23-T1-A to C23-T1-E red) decreases in quartz, plagioclase, K-feldspar and sillimanite, and increases in biotite, and muscovite. The mineral content of the second analyzed layer (C23-T1-I to C23-T1-E green) decreases in quartz, plagioclase, biotite, K-feldspar and sillimanite but increases in muscovite and albite. Thermodynamic modelling reveals the rock was likely undersaturated during at least part of the deformation phases. Minor, trace and RE-element analysis reveals a mass transfer, just like with the Cala Sardina samples. From sample C23-T1-D a total mass change of +11.1% is calculated compared to "unaltered" sample C23-T1-A. For sample C23-T1-F a total mass change of -9.69% is calculated compared to "unaltered" sample C23-T1-I.

	Cala Sardina	**Tudela**
Distance: Distal-proximal samples	88 cm 100cm – 12cm from shear zone	20 cm 20cm - <1cm from shear zone
Strain-range: Distal-proximal samples	0.0-3.2	0.7-114.1
Main **structural difference** between distal and proximal samples	Distal samples show 2 foliations with the first one being dominant. Proximal samples show only the second foliation which is perpendicular to the shear zone, completely overprinting the first one	Distal samples only show 1 foliation. Proximal samples show two foliations, the second one being perpendicular to the shear zone and becoming more dominant towards the shear zone.
Main **mineralogical difference** between distal and proximal samples	Samples show an increase in muscovite, plagioclase and chlorite towards the shear zone.	Distal samples contain K-feldspar blast, these are no longer observed in proximal samples.
Notes from **thermodynamic modelling**	Likely H2O saturated during deformation	Likely H2O undersaturated for at least part of deformation
Total mass transport in proximal sample compared to distal sample	+8.14%	-9.69% +11.1%

Table 4.1: Overview comparing the two sampled shear zones for the core findings of this research.

4.1 SEM workflow methodology

The Scanning electron microscope in combination with the Automated mineralogy workflow used for this research is relatively new, and therefore the results from this workflow need to be studied closely and are (if possible) cross-checked and verified with other available data and analytical techniques.

First it must be noted that during scanning a software issue occurred that stitched scanned "tiles" of the thin sections together. This caused a minority of the pixels in the 5% overlapping

regions of the “tiles” to become mixed compositions of either tile, giving some areas a wrong chemical signature and thus a wrong mineral classification.
Some of the scanned “tiles” also have a lower scanning resolution than required, this results in some grains having a wrong identification (for example; plagioclase grains in the Tudela thin sections are classified as Albite in these tiles).
Both these errors are visible in the color maps, the stitching of the tiles mostly in the Cala Sardina samples (fig. 3.7 and 3.8 and appendix I, II), the tiles with lower resolution in the Tudela scans (fig. 3.12, 3.13, 3.14 and appendix III, IV, V).
These issues resulted in unclassified or misclassified grains, thereby introducing additional error in the mineral proportions (tables 3.5 and 3.7). As this misclassification of pixels only occurred in the area of overlap, the overall impact on the bulk composition is expected to be minimal. This is further supported by comparing the BRC calculated with the SEM-AM method with the BRC obtained with the XRF, which show only small differences (under 10% for the major oxide weight percentages in the Cala Sardina samples and up to 20% in the Tudela samples, see tables 3.4 and 3.6). Because of this the BRC from the SEM-AM was deemed useable, but this error should be kept in mind when reviewing the data.

Polymorphic minerals (such as sillimanite/andalusite/kyanite) all have the same chemistry and thus are all identified as the same mineral by the AM but indicate different PT-conditions. Thus to obtain a realistic overview of the mineral content a manual check of the chemical composition of scanned minerals and a separate optical microscopy study of the samples was performed.

A last note of caution is that the SEM-AM BRC is based on a small 2D surface, where the assumption is made that this surface is representative for the entire rock sample. In isotropic rocks, for instance if the rock is strongly banded in composition (as is the case for the samples used in this study) or if minerals present have a preferred orientation in the rock (such as phyllosilicates), the chosen section will impact the calculated BRC and may not be representative for the actual total rock BRC.
An additional influence on the representativeness is the size of the area that is scanned with SEM-AM. For the C23-S1-A sample a scan of a small area (~ 15%, deemed representative) and a scan of >40% of the entire thin section were made. BRC for both scans were compared with the C23-S1-A XRF obtained BRC and the larger SEM-scan gave a BRC result much more similar to the XRF-BRC. Based on this, a minimum thin section area of at least 40% was chosen for all samples scanned.

4.2 Deformation, foliation, and bulk rock composition

For the validity of this research the sampled lithological layers (fig. 3.1 and 3.2) for both localities need to be compositional layers. If the composition of these layers is not homogeneous before deformation the study of compositional changes with increased strain (further and closer) to the shear-zone is invalid as the composition was never the same to begin with.

As the Cap de Creus area has experiences multiple deformation stages there are 3 main foliations visible in the field; the sedimentary layering formed at deposition Ss and the S1 schistosity related to the first deformation phase, which are often subparallel and referred to as Ss/1 in literature (Druguet, 1997, 2001), in this research these will be called S1. S2 is related to a second deformation phase characterized by E-W folding of the S1, and S3 is related to the third deformation event of shearing under greenschist conditions (Druguet, 1997, 2001).
Based on the field relations the sampled layers and measured foliation was determined to represent S2, namely the compositional layer S1 transposed by D2. Subsequently, this S2 is deformed due to D3 shearing, resulting in shear bands and S-C and C’ fabrics proximal to the shear zone. This would mean the sampled layers are indeed deformed Ss layers, making them compositional layers.

Bulk rock compositions for both localities show very little differences in oxide weight percentages at different sample point (see table 3.4 and 3.6). Thus the sampled layers have a very homogeneous composition over the sampled distance, which would argue in favor of the hypothesis that the sampled layers are composition layers.

In the Cala Sardina thin sections 2 different foliations are observed; a prominent first foliation parallel to the layering in the field and thus likely S2, and a crenulation foliation overprinting this first foliation (fig. 3.3 and 3.10). The crenulation foliation is parallel to the shear zone and likely results from the D3 shear zone deformation, making this foliation S3 (fig. 3.10).
These two foliation directions have an angle of around 75° in thin section C23-S1-A, ~45° in thin section C23-S1-B, ~30° in C23-S1-C and ~20°in the most proximal sample C23-S1-D (fig 3.3), with S3 oriented sub-parallel to the shear zone foliation. Thus the two foliations become aligned closer to the shear zone with only S3 visible in the most proximal thin sections.

The Tudela thin sections also show 2 foliations; the most distal samples only show one foliation that aligns with the observed compositional layering, likely S2. Closer to the shear zone, from around 9 cm distance and a strain value of 3.8, another foliation is observed, with an angle of around 70° to S2 (fig. 3.7). This angle become smaller closer to the shear zone. This second foliation is roughly sub-parallel to the shear zone and thus likely S3. In samples C23-T1-E the S3 makes an abtuse angle to the shear zone foliation, as the S3 foliation is defined by extensional C' foliation.

It is concluded from this data that the sampled layers can indeed be interpreted as compositional layers that follow Ss/1 (compositional layering) deformed by S2 and later S3, that have very homogeneous bulk rock compositional along strike.

4.3 Changes in mineralogy

4.3.1 Cala Sardina

The Cala Sardina samples contain nodules of muscovite with epidote cores. This nodule-muscovite shows a different CPO than the muscovite found in the matrix of these samples. The nodules also show no (distal samples) to little (proximal samples) signs of deformation while adjacent muscovite/biotite layers are strongly deformed and observed bending around the nodules. The weaker nature of muscovite would make them deform, had they existed during the deformation responsible for the folding of the quartz layers and the bending and braking of the primary biotite and muscovite.
These observations suggest that the muscovite in the nodules formed after the bulk of the deformation had happened. A possible explanation is that these nodules consisted of a stronger mineral during deformation, which was subsequently replaced by muscovite (+-epidote). Alternatively, it could be that the muscovite nodules, due to their grain size difference with respect to the surrounding matrix, were relatively too strong to be deformed, with deformation focusing on the finer grained matrix instead.

The Cala Sardina samples were taken from the Punta dels Fallarons magmatic complex. SEM-scanned samples from Punta dels Farallons (not influenced by the shear zones) studied by Kok (2022) show large quartz, plagioclase, K-feldspar and garnet crystals.
It is therefore possible that in the Cala Sardina samples, the original nodule mineral was K-feldspar, which would be able to withstand the applied strain during shearing and later, under the right H2O saturated conditions, form a retrograde phase reaction into muscovite.
Reactions responsible for the formation of the K-feldspar blasts in this metamorphic zone are, according to Druguet (1997):

$$Ms + Ab + Qtz => Kfs + Sill + H2O$$
and/or
$$Ms + Qz => Kfs + Sill + H2O$$

These phase reactions are found in quartz-saturated KASH systems at approximately 730°C and 6.1 kbar (Spear et al., 1999).
The retrograde formation of muscovite involves hydration of K-feldspar, often reacting with sillimanite into muscovite and quartz (Pryer and Robin, 1995; Peterman and Grove, 2010). Some sillimanite was definitely present in the sample, as it is still observed in SEM-scans (fig. 4.10) and through optical microscopy, which supports this theory.

The epidote observed in the muscovite-nodules shows a chemical signature similar to clinozoisite. Abundant clinozoisite is found in Cap de Creus shear zone samples of van Melick (2021), who relates this occurrence to feldspar alteration in combination with influx of Ca-bearing fluids. No large concentrations of calcium are observed in analysis of the Cala Sardina samples (table 3.4). Thus no explanation is yet found for the occurrence of this mineral in the cores of these nodules, and more research is needed to do so.

4.3.2 Tudela

The Tudela samples are part of the Cap de Creus sillimanite-K-feldspar zone as described by Druguet (1997). The samples furthest from the shear zone (C23-T1-A and C23-T1-I) contain K-feldspar blasts (fig 3.9 and 3.10).
The K-feldspar blasts in distal samples are overgrown by plagioclase, quartz and biotite and completely disappear with proximity to the shear zone (sample C23-S1-E, fig 3.11). This is also visible in the K-feldspar mineral wt%, decreasing from 2.45 in T1-A to 0.97 in T1-E (red) and from 2.06 in T1-I to 0.55 in T1-E (green) (table 3.7). This suggests the retrograde reaction of K-feldspar into other components.

As discussed before, the retrograde hydration reaction of K-feldspar often involves sillimanite and produces muscovite and quartz. From distal samples, where K-feldspar still exist, to proximal samples, where it has almost entirely reacted away, there is a slight decrease in sillimanite (1.01 wt% from T1-A to T1-E and 0.51 wt% decrease from T1-I to T1-E, table 3.7) and an increase in muscovite (4.03 wt% increase from T1-A to T1-E and 3.09 wt% increase in T1-I to T1-E, table 3.7) which supports this theory.

In distal samples K-feldspar is mostly overgrown by quartz and plagioclase, with no signs of muscovite. This lack of muscovite suggests a different retrograde reaction of K-feldspar is taking place, resulting in quartz and/or plagioclase.

4.4 P-T paths and deformation timing

As mentioned in section 1.2.2. the Cap de Creus area experienced 3 main deformation phases;

- D1: The oldest deformation phase which is responsible for the first widespread schistosity in the area (S1) defined by alignment of phyllosilicates in the metasedimentary rock. It is associated with crustal thickening. Metamorphic conditions are estimated to not have exceeded greenschist facies conditions (Druguet 2001)
- D2: A prograde folding event, characterized by folding of S1 in prograde metamorphic conditions up to peak metamorphism. Associated foliations (S2) are mainly defined by preferred orientation of biotite and sillimanite growth.
- D3: The deformation phase associated with the studied shear zones, characterized by progressive deformation under retrograde metamorphic conditions.

As discussed in section 4.2 two foliations are observed in our rock samples, with the first prominent foliation likely being S2 and the crenulation foliation parallel to the shear zones likely S3.

4.4.1 Cala Sardina

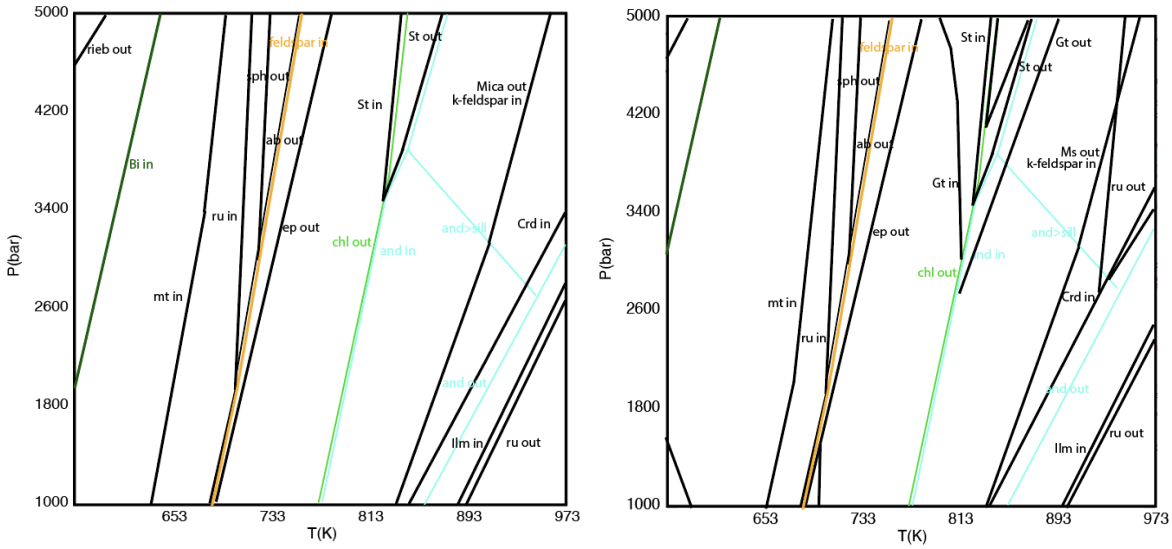

Figure 4.1: Modelled psuedosection for Cala Sardina sample C23-S1-A, left shows the model based on SEM+AM-BRC and right shows the model based on XRF-BRC.

The Cala Sardina samples were taken from a shear zone in the Punta dels Farallons migmatite complex, where the PT-conditions are poorly constrained from literature. Druguet (1997) suggests peak temperatures above 700 °C and pressures up to 7.4 kbar for this complex, which are extremely high-pressure values compared with the adjacent sillimanite zone. A study by Kok (2022) suggests peak-conditions of ~700 °C and 4.5-5.0 kbar, but further research into more precise measurement is suggested.

Timing	First	Peak PT	Retrograde	Last
Minerals	Quartz Biotite Plagioclase Muscovite	*K-feldspar* + Sillimanite	Muscovite II Epidote	Chlorite
PT-conditions	>380°C	>620°C >3 kbar	<400 °C	<550°C
Deformation phase	D1	D2	D3	D3

Table 4.2: Summary of observed mineral growth timing in Cala Sardina samples, associated PT-conditions and likely associated deformation phase.

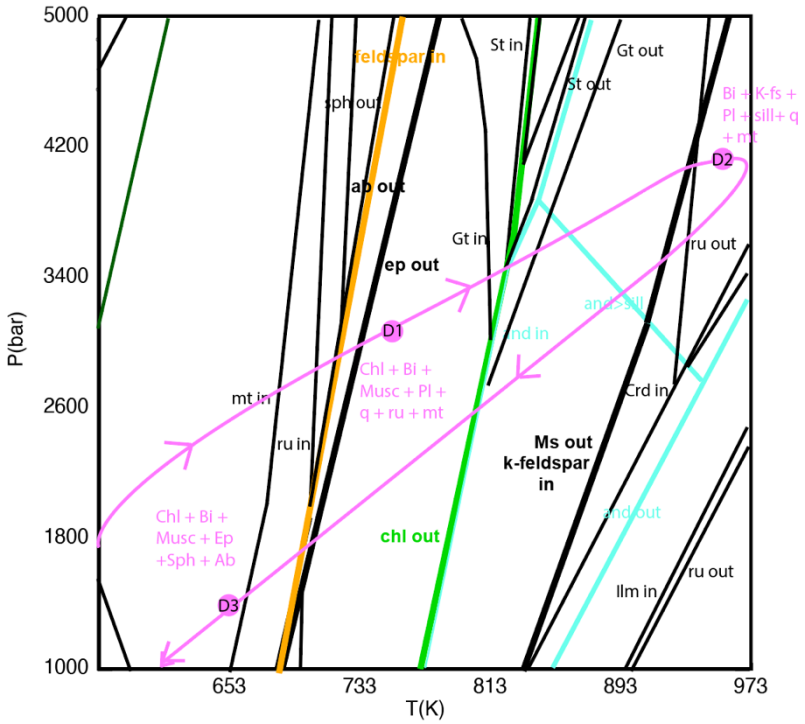

Figure 4.2: Modelled psuedosection of C23-S1-A -XRF and assumed PT-path (pink line) from found mineral assemblages (marked with pink circles) and likely associated deformation phases.

The primary minerals that make up the matrix of the Cala Sardina rocks are Qz+Bt+Pl+Ms, fitting modelled temperature conditions between 380°C-620°C at all modelled pressure values. Grains from this matrix follow S2 foliation. The estimated temperature conditions match those estimated by Druguet (2001) for the Cap de Creus-D1 deformation phase, around 450°C and 2-5 kbar pressure.

The later formed K-feldspar that, if the hypothesis is correct, initially formed the muscovite-nodules, indicates temperatures above 620°C at all modelled pressure conditions. The growth of sillimanite over the matrix grains indicates pressure conditions above at least~3 kbar and temperatures above 560°C. These two minerals show no clear growth relation (due to the K-feldspar being replaced) but likely grew together due to overlapping growth conditions. The K-feldspar and sillimanite would indicate the peak metamorphic conditions observed in the samples, and would agree with estimates of Druguet (1997) and Kok (2022) as mentioned above. As indicated by Druguet (2001) these conditions match the D2 phase.

The transformation of the K-feldspar nodules into muscovite indicates temperatures below ~620°C, and thus a drop in temperature conditions. Post-K-feldspar muscovite grains do not align with S3 foliations and are only slightly deformed proximal to the shear zone, which likely makes the origin of these grains late D3. Late D3 conditions are estimated at 430°C and 3 Kbar by Druguet (2001). The question that remains is; if the retrograde reaction of K-feldspar to muscovite can happen already at temperatures below 650°C, why did it not happen during an earlier (hotter) D3 phase?

The chlorite overgrowing all previous minerals indicates a temperature below 550°C, continuing the drop to lower PT conditions. All information summarized in table 4.2. All PT-conditions and the possible path connecting them drawn in figure 4.2.

4.4.2 Tudela

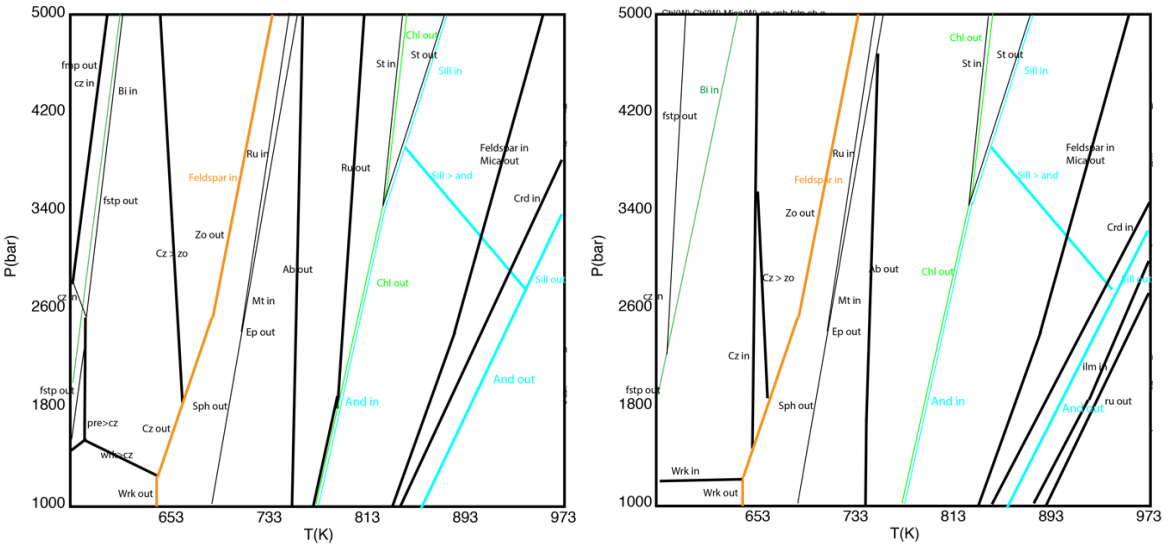

Figure 4.3: Modelled psuedosection for Tudela sample C23-T1-A, left shows the model based on SEM+AM-BRC and right shows the model based on XRF-BRC.

The Tudela samples were taken from the Cap de Creus sillimanite k-feldspar zone. Peak conditions for this zone are estimated at 670°C and 4.7 kbar by Druguet (2001) and at 650±30°C and >3.9kbar by van Melick (2021).

Timing	First		Peak PT	Retrograde	Last
Minerals	Plagioclase Quartz Biotite	Muscovite Sillimanite	K- feldspar	Biotite Plagioclase	Albite Quartz
PT-conditions	>380 °C	>560 °C >3.1 kbar	>620 °C >2.9 kbar	>380 °C	<470 °C
Deformation phase	D1	Early D2	D2	D3	D3

Table 4.3: Mineral growth timing observed in Tudela samples, associated PT-conditions and likely associated deformation phase.

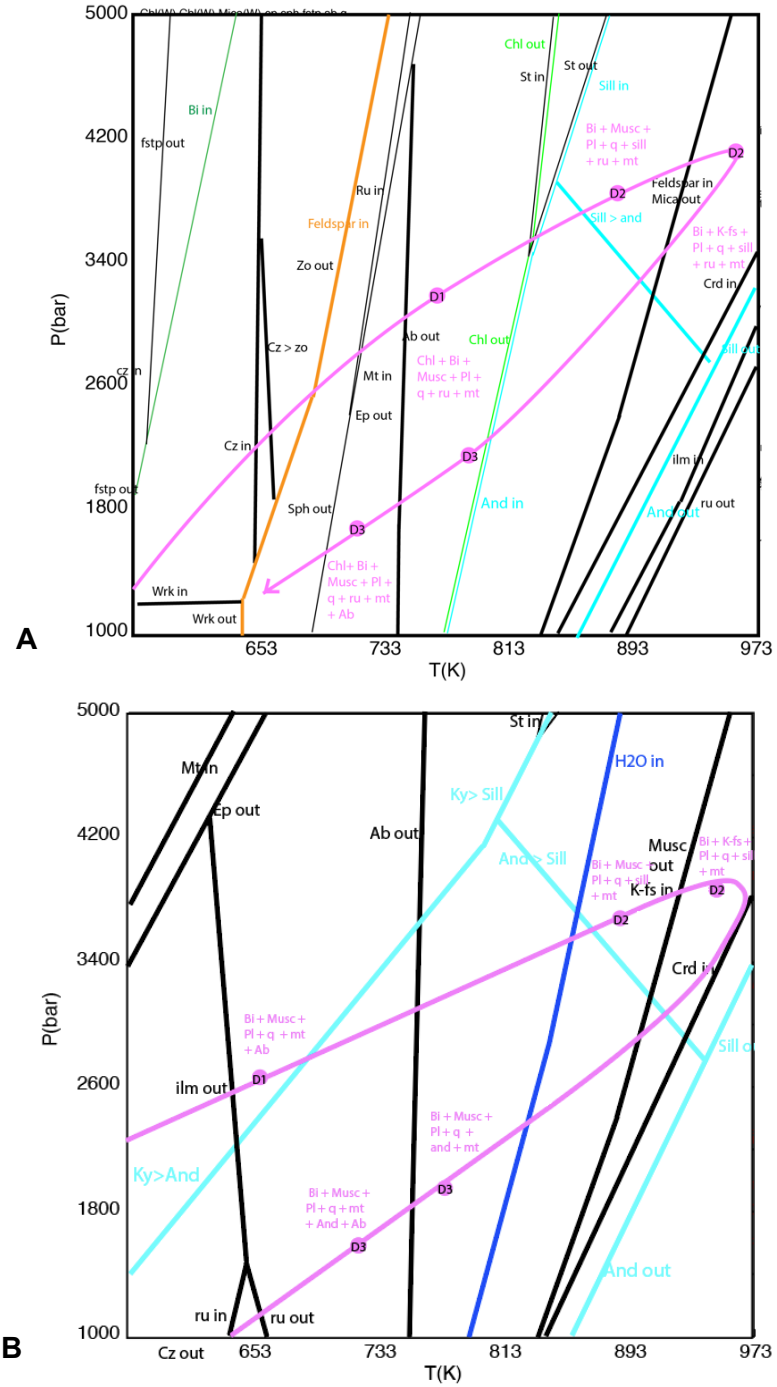

Figure 4.4: Modelled psuedosections of C23-T1-A-XRF and assumed PT-path (pink line) from found mineral assemblages (marked with pink circles) and likely associated deformation phases. Figure A shows the model saturated with H2O, figure B shows the undersaturated model with only 1 wt% H2O.

Growth relations observed in SEM-scans and thin sections suggest the earliest minerals present in the rock are plagioclase, quartz and biotite, suggesting temperatures of above 380°C, matching conditions of D1.
Biotite crystals are then overgrown by muscovite and sillimanite, indicating a rise in temperature and pressure to >560 °C and >3.1 kbar, indicating that these minerals were likely formed during early D2 (Druguet 2001).
All previous grains are then overgrown by K-feldspar blasts, indicating even higher conditions of >620 °C and >2.9 kbar, matching the estimates of peak conditions during D2 of Druguet (2001).

These K-feldspar blasts are overgrown with biotite and plagioclase, indicating conditions of >380 °C and the start of retrograde deformation taking place during D3. The last minerals to grow are albite and quartz which shows a subsequent cooling of temperatures to at least below 470 °C. All these findings are summarized in table 4.3. All found PT-conditions and a possible path connecting them (in saturated in undersaturated water conditions) shown in figure 4.4.

It must be noted that the amount of albite found in the samples is limited, closer inspection of SEM-phase maps shows that many pixels identified as albite are found in "tiles" scanned with lower resolution, as mentioned in section 4.2, and thus are likely plagioclase. This makes the amount of albite noted in table 3.7 much too high. Closer inspection of SEM-phase maps for Tudela (for example figure 3.14) reveals traces of albite inside or on the rim of plagioclase grains, outside of the "faulty tiles", and thus proves some albite is present in these samples. This albite is also found to grow in or around the later generation of plagioclase, showing that it is formed in retrograde reactions and not a remnant of prograde metamorphism.

Following the described PT conditions and the modelled saturated psuedosections (fig 4.4a) for these samples one would expect to find some chlorite to form under retrograde conditions in which the albite is formed, but this is not the case (or at least only a very small amount). One possibility for this, as mentioned in result section 3.3.3 and shown in figure 4.4b, is the undersaturation of H_2O during deformation, which will be further discussed in section 4.5.

4.5 Influence of fluids

In both the Cala Sardina and Tudela samples minerals that are indicators of retrograde metamorphism are found, being in line with literature on the Cap de Creus metamorphic history and the retrograde origin of the shear zones found there (Druguet, 1997; Fusseis et al., 2006; Carreras et al., 2010). Retrograde metamorphism often involves the (re)introduction of fluids, which helps the transformation of high-grade into lower grade metamorphic minerals (Corbett and Phillips, 1981; Kelemen and Hirth, 2012). The extent of the hydration and thus amount of retrograde overprinting of minerals is in part controlled by the amount of water that can infiltrate the rocks (Pryer and Robin, 1995). The Cap de Creus shear zones were active during lower grade PT conditions and were a conduit for the reintroduction of fluids into the rock, aiding in the retrograde overprinting of the rocks close to the shear zone (Gibson, 1990; Carreras, 2001).

Comparing distal to proximal samples from these shear zones an increase in retrograde or hydrated secondary minerals can be found, such as chlorite, muscovite and epidote in the Cala Sardina samples and albite and muscovite in the Tudela samples. This shows there is more retrograde overprinting, and likely more input of water closer to the shear zone.

In the Cala Sardina samples there is, next to the increase in hydrated minerals, a total mass transport of +8.4%. This means 8.4% of the mass has changed between the distal and proximal sample (a distance of 88 cm and a change in strain value of 3.2). This mass transport is aided by water. This shows the Cala Sardina low strain/distal samples experience less water input then the high strain/proximal samples. This is backed up by van Melick (2021) who finds ±54% mass transfer by fluids of samples taken in (deformed) and outside (undeformed) of the Cap de Creus shear zones.

In the Tudela samples there is a smaller increase in hydrated minerals. Interestingly there are high-grade K-felspar grains visible in the more distal samples (20 cm from the shear zone) which are completely overprinted by lower grade minerals in the most proximal samples (<1 cm). This shows a large difference in amount of retrograde overprinting on this relatively small distance.

The total mass change between the distal and proximal tudela samples is -9.69% to +11.1%. over a distance of ~20 cm. This is a slightly larger amount of mass change than found in the Cala Sardina samples over a smaller distance. Individual element concentration-ratio's also show larger values than the Cala Sardina ones, showing that there is a larger difference in water input between distal and proximal samples for the Tudela samples.

The retrograde reaction of K-feldspar into muscovite, quartz and possibly albite is a hydration reaction and thus needs water added to the system to be able to happen. So low water input for the distal samples could explain why K-feldspar blast are still present in the Tudela distal samples, but have reacted away in the more proximal samples which experienced more water input.

The Tudela samples contain almost no chlorite, with the exception of some traces in the proximal samples, which would be highly expected in these samples when looking at modelled saturated psuedosections (fig 4.4a). A theory for the lack of chlorite can be found in the modelled undersaturated psuedosections (fig 4.4b) which do not show any possibility for chlorite to form. The unexpectedly low amount of chlorite could thus be explained by an undersaturated environment in the Tudela samples.
Another explanation for the lack of chlorite is proposed by van Melick (2021) who suggest the amount of chlorite is controlled by the amount of iron and/or magnesium available rather than the amount of water. Looking at table 3.7 and Tudela SEM-phase maps shows these samples contain small amounts of tourmaline, definitely less than the Cala Sardina samples (table 3.5) in which chlorite is found in abundance, aiding this theory.
Alternatively, the samples could have been deformed under saturated conditions but at temperatures too high for chlorite to form (i.e. >~500 °C).
The lack of structural overprinting in distal Tudela samples, where no foliation related to the shearing can be found at 13 cm from the shear zone, can possibly also be explained by the lack of water input observed here. But further study on this subject is suggested.

It is concluded that there is more water input in proximal samples than distal samples for both shear zones. This is seen in the Cala Sardina samples over a distance of 100 cm in the difference of hydrated minerals and mass transport. This difference in water input is larger for the Tudela samples over a distance of ~20 cm, where the most distal samples were likely undersaturated. As the Cala Sardina samples were taken form a larger scale shear zone than the Tudela samples, the size of the shear zone is likely of influence on the difference in water supply. A larger shear zone means a larger conduit of water and thus more saturated conditions.

4.6 Shear zone activation timing and conditions

As mentioned in the introduction, the leading theory is that is the D3-deformation/shearing and greenschist overprinting of the higher-grade metamorphic rocks of Cap de Creus happened during the late retrograde stages of the Variscan orogeny (Carreras, 2001; Druguet et al., 2014). This is questioned by Vissers (2017) who suggests a Jurassic origin of the shear zones and an Alpine reactivation of them.

The Cala Sardina samples show muscovite nodules that appear to be unaffected by the shearing that these samples enjoyed. As proposed in section 4.3 this could suggest the presence of K-feldspar which would be able to withstand the applied strain. These K-feldspar grains would then be transformed to muscovite after- or in the latest stages of shearing, because if they had transformed during or before shearing the muscovite would appear deformed.
The retrograde reaction from k-feldspar to muscovite happens at ~620°C in modelled psuedosection (figure 4.2), i.e. definitely at higher temperatures than estimated for D3 by van Melick (2021) and Druguet (2001), which suggest a maximum of 400-430 °C at 2.5kbar. So, the question is then, why did these nodules only transform during the latest stages of shearing?

A possibility for the k-feldspar to muscovite retrograde reaction taking place at lower conditions than expected is a lack of water during deformation. This retrograde phase reaction needs H2O to happen (as mentioned in 4.3.1) and can thus be stalled by undersaturated conditions during the earlier shearing stages. As shear zone formation progressed they became a better conduit for external fluids, finally resulting in enough fluids for this phase reaction during the latest D3 phases.
This is also seen in the even later occurrence of chlorite, which overgrows all previously formed minerals and does not align with the S3 foliation observed, suggesting that all chlorite formed after shearing has stopped. This in turn could mean that the shear zone only reached chlorite conditions after shearing has already taken place, and the shear zones just act as a conduit for the formation of retrograde chlorite.

The Tudela samples show K-feldspar blasts as well, which are still visible at 20 cm from the shear zone, but have reacted away closer to the shear zone. Here it seems only the more proximal samples have had enough water for the retrograde phase reaction of K-feldspar to muscovite to take place. This shows there was an introduction of water closest to the shear zone, but an overgrowth of retrograde chlorite is still missing.
This could suggest the retrograde phase reaction of k-feldspar (and thus an influx of water) has happened at temperatures above chlorite conditions. At lower conditions, when a retrograde reaction of albite took place, the shear zone was undersaturated, prohibiting the formation of chlorite. This would mean that in the later stages of shearing the shear zone was a worse conduit of water.
Another possibility is that a lack of iron and/or magnesium prohibited chlorite formation, and not a lack of water. Mineral growth relations in these samples do not give a clear indication of timing and/or which theory is correct.

Overall it is concluded that mineral growth in these samples do not necessarily reflect early-D3 shearing stages. This is likely because a lack of water influx prohibited the retrograde metamorphism during these stages of deformation.
As Vissers et al. (2017) used $^{40}Ar/^{39}Ar$ dating of retrograde white mica from the Cap the Creus shear zones, it could be that they found a much younger age of the shear zones as these retrograde white micas are only formed during later stages of deformation, when water was abundant. The middle Jurassic age found could thus reflect a later stage of shearing or reactivation during this time, but not the initiation of these shear zones.
Thus the data in this thesis suggests the origin of these shear zones could well be before the Jurassic, indicating that the hypotheses of Druguet and Carreras that they originated in the later stages of the Variscan orogeny could be correct.

5. Conclusion

- The SEM-AM technology used in this research provided usefull mineralogical and chemical data for the analysis performed. Bulk Rock Composition (BRC) calculated by SEM-AM and XRF both resulted in very similar psuedosections and similar PT-conditions for all samples. Caution needs to be taken when scanning smaller sections as BRC can be not representable for the total rock.

- Modelled psuedosections and mineralogical assemblages for both sampled areas show first an increase in PT conditions, in line with Cap de Creus D1 and D2 formation phases, and later a retrograde path during D3-shearing deformation. Both sampled shear zones show significant changes in mineralogy when looking at distal vs proximal samples. The proximal samples showing lower-grade mineral assemblages than the distal samples and more hydrated minerals in both cases. Thus both shear zone show a more prominent overprint of retrograde metamorphism in high-strain/proximal samples than low- strain/distal samples.

- Samples from the Cala Sardina shear zone show that the bulk of the observed shear deformation took place before the retrograde overprinting of muscovite. From this it is concluded that mineral growth in these samples do not reflect the youngest (early D3) Cap the Creus shearing stages. And formation of retrograde muscovite took place when shear zones were already established and likely conduits of water.

- If retrograde overprinting of muscovites took place as shear zones were already established, as this work suggests, the $^{40}Ar/^{39}Ar$ dating of retrograde white micas done by Vissers et al. (2017) will reflect the shear zone ages poorly, and likely only indicates a later stage of shearing or reactivation during this time, but not necessarily the initiation of these shear zones. This favors the theory of Druguet and Carreras on the Cap the Creus shear zones being of late-stage Variscan origin in the ongoing discussion surrounding this subject.

- Water input through the shear zones appears essential for the retrograde overprinting of previous high-grade mineral assemblages, explaining lower grade assemblages closer to the shear zone. Values of distance and strain (with respect to the shear zone) seem of no correlation to the amount of water input. Scale of the shear zone seems more important, in which a larger, well developed, shear zone would provide a larger input of water.

Bibliography

Ague, J.J. 2003. Fluid infiltration and transport of major, minor, and trace elements during regional metamorphism of carbonate rocks, Wepawaug Schist, Connecticut, USA. Am. J. Sci. 303(9): 753–816. doi: 10.2475/ajs.303.9.753.

Carreras, J. 2001. Zooming on Northern Cap de Creus shear zones. J. Struct. Geol. 23(9): 1457–1486. doi: 10.1016/S0191-8141(01)00011-6.

Carreras, J., and I. Capella. 1994. Tectonic levels in the Palaeozoic basement of the Pyrenees: a review and a new interpretation. J. Struct. Geol. 16(11): 1509–1524. doi: 10.1016/0191-8141(94)90029-9.

Carreras, J., D.M. Czeck, E. Druguet, and P.J. Hudleston. 2010. Structure and development of an anastomosing network of ductile shear zones. J. Struct. Geol. 32(5): 656–666. doi: 10.1016/j.jsg.2010.03.013.

Carreras, J., and E. Druguet. 1994. Structural zonation as a result of inhomogeneous non-coaxial deformation and its control on syntectonic intrusions: an example from the Cap de Creus area, eastern-Pyrenees. J. Struct. Geol. 16(11): 1525–1534. doi: 10.1016/0191-8141(94)90030-2.

Carreras, J., and M. Losantos. 1982. Geological setting of the Roses granodiorite (E-Pyrenees, Spain). Acta Geol. Hisp. 17(4): 211–217.

Castiñeiras, P., M. Navidad, M. Liesa, J. Carreras, and J.M. Casas. 2008. U-Pb zircon ages (SHRIMP) for Cadomian and Early Ordovician magmatism in the Eastern Pyrenees: New insights into the pre-Variscan evolution of the northern Gondwana margin. Tectonophysics 461(1–4): 228–239. doi: 10.1016/j.tecto.2008.04.005.

Choukroune, P. 1992. Tectonic evolution of the Pyrenees. Annu. Rev. Earth Planet. Sci. Vol. 20: 143–158. doi: 10.1146/annurev.ea.20.050192.001043.

Connolly, J.A.D. 2005. Computation of phase equilibria by linear programming: A tool for geodynamic modeling and its application to subduction zone decarbonation. Earth Planet. Sci. Lett. 236(1–2): 524–541. doi: 10.1016/j.epsl.2005.04.033.

Connolly, J.A.D., and M.E. Galvez. 2018. Electrolytic fluid speciation by Gibbs energy minimization and implications for subduction zone mass transfer. Earth Planet. Sci. Lett. 501: 90–102. doi: 10.1016/j.epsl.2018.08.024.

Connolly, J.A.D., and K. Petrini. 2002. An automated strategy for calculation of phase diagram sections and retrieval of rock properties as a function of physical conditions. J. Metamorph. Geol. 20(7): 697–708. doi: 10.1046/j.1525-1314.2002.00398.x.

Corbett, G.J., and G.N. Phillips. 1981. Regional retrograde metamorphism of a high grade terrain: the Willyama Complex, Broken Hill, Australia. Lithos 14(1): 59–73. doi: 10.1016/0024-4937(81)90037-2.

Druguet, E. 1997. The structure of the NE Cap De Creus peninsula. Relationships with metamorphism and magmatism.

Druguet, E. 2001. Development of high thermal gradients by coeval transpression and magmatism during the variscan orogeny: Insights from the cap de creus (Eastern Pyrenees). Tectonophysics 332(1–2): 275–293. doi: 10.1016/S0040-1951(00)00261-4.

Druguet, E., J. Carreras, and J.E. Mezger. 2018. Reply to discussion on 'middle Jurassic shear zones at cap de Creus (Eastern Pyrenees, Spain): A record of pre-drift extension of the piemonte-ligurian ocean?' J. Geol. Soc. London. 175(1): 189–191. doi: 10.1144/jgs2017-115.

Druguet, E., A. Castro, M. Chichorro, M.F. Pereira, and C. Fernández. 2014. Zircon geochronology of intrusive rocks from Cap de Creus, Eastern Pyrenees. Geol. Mag. 151(6): 1095–1114. doi: 10.1017/S0016756814000041.

Druguet, E., C.W. Passchier, J. Carreras, P. Victor, and S. den Brok. 1997. Analysis of a complex high-strain zone at Cap de Creus, Spain. Tectonophysics 280: 31–45.

Filleaudeau, P.Y., F. Mouthereau, and R. Pik. 2012. Thermo-tectonic evolution of the south-central Pyrenees from rifting to orogeny: Insights from detrital zircon U/Pb and (U-Th)/He thermochronometry. Basin Res. 24(4): 401–417. doi: 10.1111/j.1365-

2117.2011.00535.x.
Forshaw, J.B., and D.R.M. Pattison. 2021. Ferrous/ferric (Fe2+/Fe3+) partitioning among silicates in metapelites. Contrib. to Mineral. Petrol. 176(9): 1–26. doi: 10.1007/s00410-021-01814-4.
Fossen, H., and G.C.G. Cavalcante. 2017. Shear zones – A review. Earth-Science Rev. 171(January): 434–455. doi: 10.1016/j.earscirev.2017.05.002.
Fusseis, F., M.R. Handy, and C. Schrank. 2006. Networking of shear zones at the brittle-to-viscous transition (Cap de Creus, NE Spain). J. Struct. Geol. 28(7): 1228–1243. doi: 10.1016/j.jsg.2006.03.022.
Gibson, R.G. 1990. Nucleation and growth of retrograde shear zones: an example from the Needle Mountains, Colorado, U.S.A. J. Struct. Geol. 12(3): 339–350. doi: 10.1016/0191-8141(90)90018-T.
Griffin, W. L., Powell, W. J., Pearson, N. J., & O'Reilly, S. Y. (2008). GLITTER: Data reduction software for Laser Ablation ICP-MS. In P. Sylvester (Ed.), *Laser Ablation–ICP–MS in the Earth Sciences: Current practices and outstanding issues* (pp. 308–311).
Holland, T.J.B., and R. Powell. 2011. An improved and extended internally consistent thermodynamic dataset for phases of petrological interest, involving a new equation of state for solids. J. Metamorph. Geol. 29(3): 333–383. doi: 10.1111/j.1525-1314.2010.00923.x.
Kelemen, P.B., and G. Hirth. 2012. Reaction-driven cracking during retrograde metamorphism: Olivine hydration and carbonation. Earth Planet. Sci. Lett. 345–348: 81–89. doi: 10.1016/j.epsl.2012.06.018.
Kok, T., M. Drury, and R. Wessels. 2022. Petrological and mineralogical analysis of the metamorphic zones in Cap de Creus, NE Spain. (January): 1–51.
van Melick, J.H. 2021. Metamorphic conditions of the Cap de Creus shear zones (NE Spain) - Insights from an integrated petrological , electron microscopy and numerical approach.
Mezger, J.E., S. Schnapperelle, and C. Rölke. 2012. Evolution of the Central Pyrenean Mérens fault controlled by near collision of two gneiss domes. Hallesches Jahrb. 34(JANUARY 2012): 11–29.
Passchier, C.W., and R.A.J. Trouw. 2005. Microtectonics.
Pennacchioni, G. 2005. Control of the geometry of precursor brittle structures on the type of ductile shear zone in the Adamello tonalites, Southern Alps (Italy). J. Struct. Geol. 27(4): 627–644. doi: 10.1016/j.jsg.2004.11.008.
Pennacchioni, G., and N.S. Mancktelow. 2007. Nucleation and initial growth of a shear zone network within compositionally and structurally heterogeneous granitoids under amphibolite facies conditions. J. Struct. Geol. 29(11): 1757–1780. doi: 10.1016/j.jsg.2007.06.002.
Peterman, E.M., and M. Grove. 2010. Growth conditions of symplectic muscovite + quartz: Implications for quantifying retrograde metamorphism in exhumed magmatic arcs. Geology 38(12): 1071–1074. doi: 10.1130/G31449.1.
Philpotts, A., and J. Ague. 2009. Principles of igneous and metamporhic petrology. Cambridge University Press.
Piazolo, S., and C.W. Passchier. 2002. Controls in lineation development in low to medium grade shear zones: A study from the Cap de Creus peninsula, NE Spain. J. Struct. Geol. 24(1): 25–44. doi: 10.1016/S0191-8141(01)00045-1.
Platt, J.P., and W.M. Behr. 2011. Grainsize evolution in ductile shear zones: Implications for strain localization and the strength of the lithosphere. J. Struct. Geol. 33(4): 537–550. doi: 10.1016/j.jsg.2011.01.018.
Pryer, L.L., and P.Y.F. Robin. 1995. Retrograde metamorphic reactions in deforming granites and the origin of flame perthite. J. Metamorph. Geol. 13(6): 645–658. doi: 10.1111/j.1525-1314.1995.tb00249.x.
Spear, F.S., M.J. Kohn, and J.T. Cheney. 1999. P-T paths from anatectic pelites. Contrib. to Mineral. Petrol. 134(1): 17–32. doi: 10.1007/s004100050466.
Tikoff, B., V. Chatzaras, J. Newman, and N.M. Roberts. 2019. Big data in microstructure analysis: Building a universal orientation system for thin sections. J. Struct. Geol.

125(September 2018): 226–234. doi: 10.1016/j.jsg.2018.09.019.
Vergés, J., M. Fernàndez, and A. Martìnez. 2002. The Pyrenean orogen: Pre-, syn-, and post-collisional evolution. J. Virtual Explor. 8: 55–74. doi: 10.3809/jvirtex.2002.00058.
Vissers, R.L.M., D.J.J. van Hinsbergen, M. Ganerød, and C.M. Wilkinson. 2018. Reply to discussion on 'middle Jurassic shear zones at cap de Creus (Eastern Pyrenees, Spain): A record of pre-drift extension of the piemonte-ligurian ocean?' Journal of the geological society, London, 174, 289-300. J. Geol. Soc. London. 175(1): 189–191. doi: 10.1144/jgs2017-115.
Vissers, R.L.M., D.J.J. van Hinsbergen, C.M. Wilkinson, and M. Ganerød. 2017. Middle jurassic shear zones at Cap de Creus (eastern Pyrenees, Spain): A record of pre-drift extension of the Piemonte–Ligurian Ocean? J. Geol. Soc. London. 174(2): 289–300. doi: 10.1144/jgs2016-014.
Watts, M.J., and G.D. Williams. 1983. Strain geometry, microstructure and mineral chemistry in metagabbro shear zones: a study of softening mechanisms during progressive mylonitization. J. Struct. Geol. 5(5): 507–517. doi: 10.1016/0191-8141(83)90056-1.
White, S. 1979. Grain and sub-grain size variations across a mylonite zone. Contrib. to Mineral. Petrol. 70(2): 193–202. doi: 10.1007/BF00374448.
White, S.H., S.E. Burrows, J. Carreras, N.D. Shaw, and F.J. Humphreys. 1980. On mylonites in ductile shear zones. J. Struct. Geol. 2(1–2): 175–187. doi: 10.1016/0191-8141(80)90048-6.
White, R.W., R. Powell, T.J.B. Holland, T.E. Johnson, and E.C.R. Green. 2014. New mineral activity-composition relations for thermodynamic calculations in metapelitic systems. J. Metamorph. Geol. 32(3): 261–286. doi: 10.1111/jmg.12071.
Zwart, H.J. 1979. The Geology of the Central Pyrenees. Leidse Geol. Meded.: 1–74.
Zwart, H.J. 1986. The variscan geology of the Pyrenees. Tectonophysics 129(1–4). doi: 10.1016/0040-1951(86)90243-X.

Appendices

Appendix I

Photo of thin section C23-S1-A in PPL and XPL lighting, overlain with SEM-phase map.

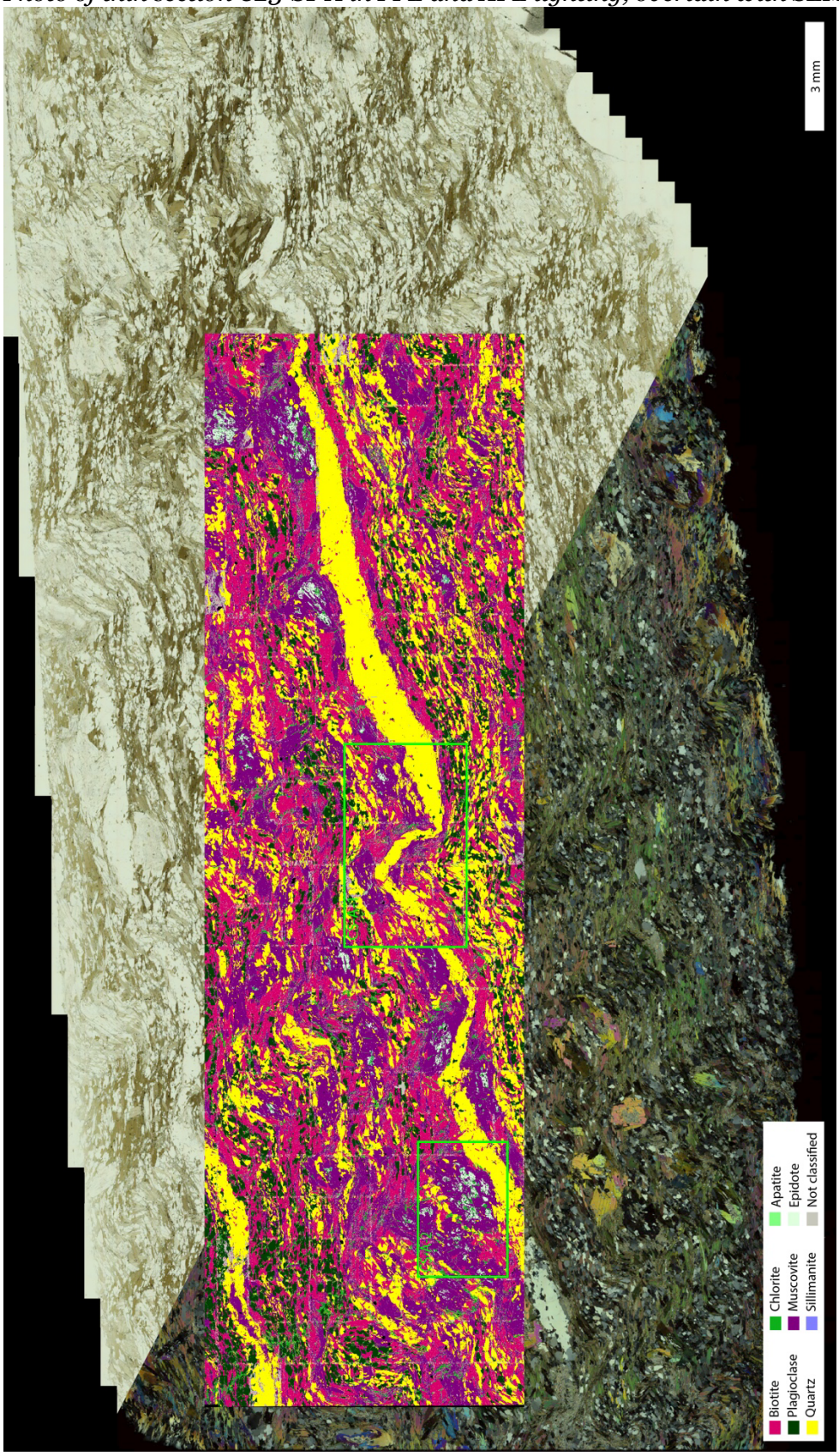

Appendix II

Photo of thin section C23-S1-D in PPL and XPL lighting, overlain with SEM-phase map.

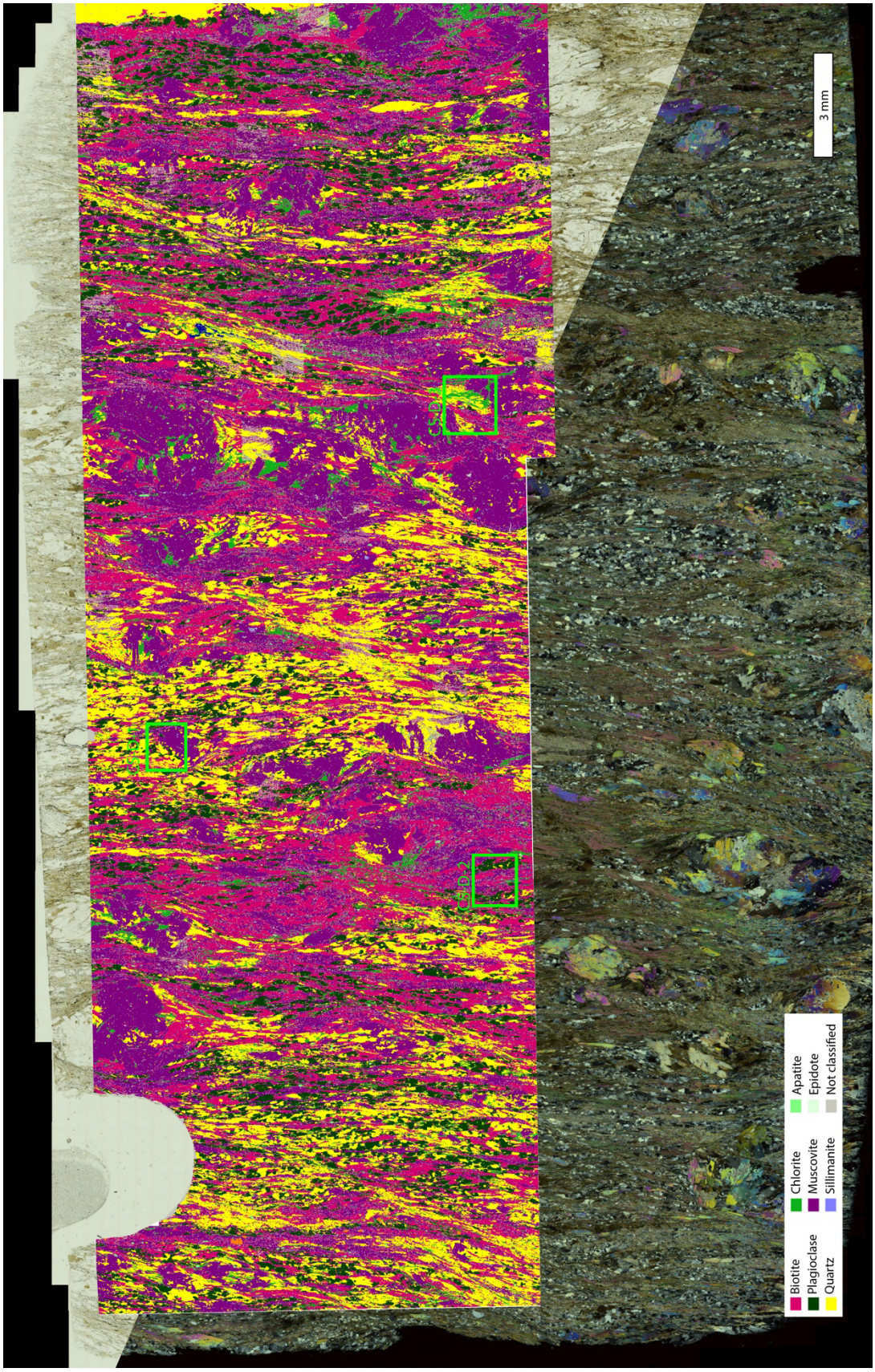

Appendix III

Photo of thin section C23-T1-A in PPL and XPL lighting, overlain with SEM-phase map.

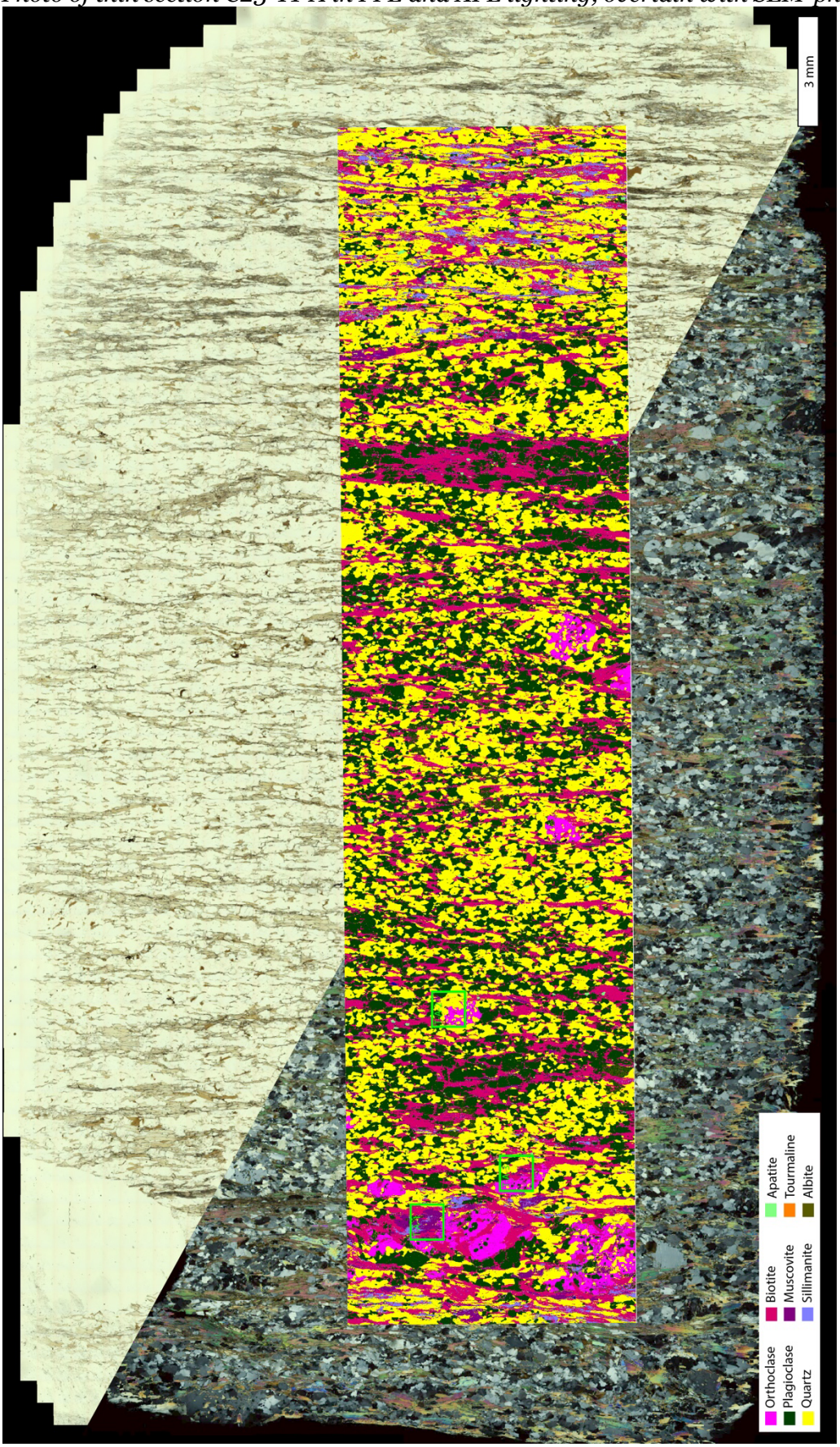

Appendix IV

Photo of thin section C23-T1-I in PPL and XPL lighting, overlain with SEM-phase map.

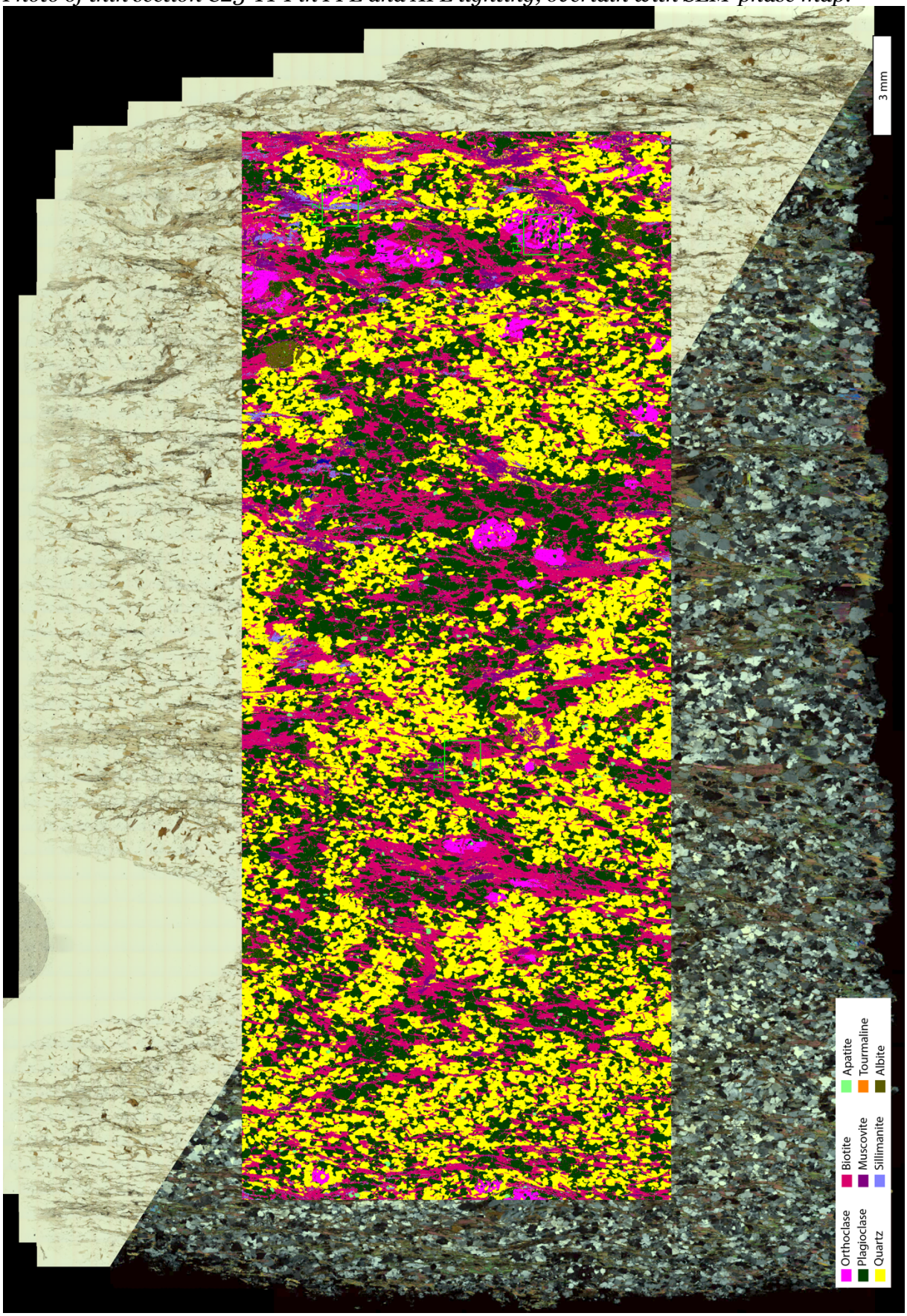

Appendix V

Photo of thin section C23-T1-E in PPL and XPL lighting, overlain with SEM-phase map.